



Article

# Sustainable Microfabrication Enhancement of Graphene Nanoplatelet-Reinforced Biomedical Alumina Ceramic Matrix Nanocomposites

Mustafa M. Nasr<sup>1,\*</sup>, Saqib Anwar<sup>2</sup>, Ali M. Al-Samhan<sup>2</sup>, Khaled N. Alqahtani<sup>1</sup>, Abdulmajeed Dabwan<sup>1</sup> and Mohammed H. Alhaag<sup>2</sup>

<sup>1</sup> Industrial Engineering Department, College of Engineering, Taibah University, Medinah 41411, Saudi Arabia

<sup>2</sup> Industrial Engineering Department, College of Engineering, King Saud University, Riyadh 11421, Saudi Arabia

\* Correspondence: mmnasr@taibahu.edu.sa

**Abstract:** Studies about adding graphene reinforcement to improve the microfabrication performance of alumina ( $\text{Al}_2\text{O}_3$ ) ceramic materials are still too rare and incomplete to satisfy sustainable manufacturing requirements. Therefore, this study aims to develop a detailed understanding of the effect of graphene reinforcement to enhance the laser micromachining performance of  $\text{Al}_2\text{O}_3$ -based nanocomposites. To achieve this, high-density  $\text{Al}_2\text{O}_3$  nanocomposite specimens were fabricated with 0 wt.%, 0.5 wt.%, 1 wt.%, 1.5 wt.%, and 2.5 wt.% graphene nanoplatelets (GNPs) using a high-frequency induction heating process. The specimens were subjected to laser micromachining. Afterward, the effects of the GNP contents on the ablation depth/width, surface morphology, surface roughness, and material removal rate were studied. The results indicate that the micro-fabrication performance of the nanocomposites was significantly affected by the GNP content. All nanocomposites exhibited improvement in the ablation depth and material removal rate compared to the base  $\text{Al}_2\text{O}_3$  (0 wt.% GNP). For instance, at a higher scanning speed, the ablation depth was increased by a factor of 10 times for the GNP-reinforced specimens compared to the base  $\text{Al}_2\text{O}_3$  nanocomposites. In addition, the MRRs were increased by 2134%, 2391%, 2915%, and 2427% for the 0.5 wt.%, 1 wt.%, 1.5 wt.%, and 2.5 wt.% GNP/ $\text{Al}_2\text{O}_3$  nanocomposites, respectively, compared to the base  $\text{Al}_2\text{O}_3$  specimens. Likewise, the surface roughness and surface morphology were considerably improved for all GNP/ $\text{Al}_2\text{O}_3$  nanocomposite specimens compared to the base  $\text{Al}_2\text{O}_3$ . This is because the GNP reinforcement reduced the ablation threshold and increased the material removal efficiency by increasing the optical absorbance and thermal conductivity and reducing the grain size of the  $\text{Al}_2\text{O}_3$  nanocomposites. Among the GNP/ $\text{Al}_2\text{O}_3$  nanocomposites, the 0.5 wt.% and 1 wt.% GNP specimens showed superior performance with minimum defects in most laser micromachining conditions. Overall, the results show that the GNP-reinforced  $\text{Al}_2\text{O}_3$  nanocomposites can be machined with high quality and a high production rate using a basic fiber laser system (20 Watts) with very low power consumption. This study shows huge potential for adding graphene to alumina ceramic-based materials to improve their machinability.

**Keywords:**  $\text{Al}_2\text{O}_3$  matrix nanocomposites; graphene nanoplatelets; clean and sustainable manufacturing; high-frequency induction heating; laser micromachining performance; surface integrity



**Citation:** Nasr, M.M.; Anwar, S.; Al-Samhan, A.M.; Alqahtani, K.N.; Dabwan, A.; Alhaag, M.H. Sustainable Microfabrication Enhancement of Graphene Nanoplatelet-Reinforced Biomedical Alumina Ceramic Matrix Nanocomposites. *Nanomaterials* **2023**, *13*, 1032. <https://doi.org/10.3390/nano13061032>

Academic Editor: Jun Shimizu

Received: 22 February 2023

Revised: 8 March 2023

Accepted: 8 March 2023

Published: 13 March 2023



**Copyright:** © 2023 by the authors. Licensee MDPI, Basel, Switzerland. This article is an open access article distributed under the terms and conditions of the Creative Commons Attribution (CC BY) license (<https://creativecommons.org/licenses/by/4.0/>).

## 1. Introduction

Ceramics have attractive properties such as high elastic stiffness, mechanical strength, biocompatibility, and stability at high temperatures, making them useful for biomedical, electronic, automotive, and aerospace applications [1]. Alumina is an example of a ceramic material that is very commonly used in a wide range of applications, such as micro-reactors [2], microfluidic devices [3], heat exchangers, heatsinks [4], and electronic substrates [3]. However, these materials have been limited by their intrinsic brittleness, high

hardness, poor electrical and thermal conductivity, and poor machinability. To overcome these challenges, alumina ceramic matrix composites reinforced with nanostructure reinforcement have been developed to create new advanced materials with unique properties that cannot be obtained using a single monolithic ceramic. Earlier attempts to fabricate ceramic matrix composites have reinforced them with ceramic or metallic particles, fibers, or whiskers [5–7]. However, incorporating alumina ceramics with these reinforcement materials cannot satisfy the requirements of their direct use as a structural component, such as in armor [8–10] or dental implants [11]. With the emergence of graphene, it has become the ideal nanostructure filler for improving the toughness, brittleness, and electrical and thermal conductivity of metal/ceramic-based nanocomposites [12–15]. This is because graphene inhibits grain growth, and the network distribution of graphene reinforcement enhances ceramic conductivity [11,16].

In the recently published literature on using graphene for reinforcing ceramic-based nanocomposites,  $\text{Al}_2\text{O}_3$  matrix nanocomposites have been of particular interest since they have exhibited improvements in mechanical properties and thermal and electrical conductivity compared to pure ceramic matrices [17–22]. For instance, He et al. [23] presented the first study on GNP-reinforced alumina ceramic matrix composites. Graphene was successfully incorporated into the alumina matrix using the ball-milling technique and then sintered by spark plasma sintering (SPS). They showed that adding graphene to the alumina matrix prevented grain growth during sintering, resulting in a fine-grained structure. Wang et al. [24] fabricated alumina composites with 2 wt.% GNS using mechanical stirring and SPS processes. The results showed that the fracture toughness of the graphene/alumina nanocomposites increased by 53% with the addition of 2 wt.% GNS compared to monolithic alumina. Furthermore, the GNS-reinforced  $\text{Al}_2\text{O}_3$  composites resulted in the refinement of the alumina grain size. This may be attributed to the nanosheets inhibiting the growth of the grain during sintering. Porwal et al. [25] fabricated graphene nanoflake (GNF)-reinforced alumina nanocomposites using a powder metallurgy technique. In their study, 0.2 wt.%, 0.5 wt.%, 0.8 wt.%, 2 wt.%, and 5 wt.% GNF/ $\text{Al}_2\text{O}_3$  specimens were prepared by a liquid phase exfoliation method and then consolidated using the SPS technique. They reported that the fracture toughness of the GNF/alumina nanocomposites increased by 40% with the addition of only 0.8 wt.% GNF. Chen et al. [26] produced GNP/ $\text{Al}_2\text{O}_3$  composites with 0.1 wt.%, 0.2 wt.%, 0.5 wt.%, and 1 wt.% GNP contents utilizing the hot pressing process. Their results indicated that the addition of GNPs improved the fracture toughness of the composites by 43.5% higher than that of the monolithic alumina. Liu et al. [27] produced GNS/ $\text{Al}_2\text{O}_3$  with 0.1 vol.%, 0.3 vol.%, 0.6 vol.%, 2.0 vol.%, and 3.5 vol.% contents using the ball-milling method and spark plasma sintering. They reported that the GNS/ $\text{Al}_2\text{O}_3$  nanocomposites exhibited higher fracture toughness, flexural strength, and Vickers hardness by approximately 25%, 103%, and 26%, respectively, compared to monolithic alumina. Ahmad et al. [10] fabricated highly dense graphene nanosheet-reinforced alumina nanocomposites using a high-frequency induction heating system (HFIHS). They studied the effects of the GNS on the nanocomposites' hardness, elastic modulus, fracture toughness, and microstructure. The obtained results showed that the addition of 0.5 wt.% GNS contents significantly improved the hardness and fracture toughness compared to the other samples. Kim et al. [28] fabricated GNP/ $\text{Al}_2\text{O}_3$  nanocomposites using the high-energy ball-milling process and high-frequency induction heated sintering. They reported that the addition of 1 wt.% and 3 wt.% graphene contents to alumina led to significant improvement in the hardness and fracture toughness of the fabricated composite. Liu et al. [29] used the ball-milling process and a pressureless furnace to fabricate  $\text{Al}_2\text{O}_3$  nanocomposites reinforced with 0.75 vol.%, 1.3 vol.%, and 1.48 vol.% GNP contents. They reported that the 0.75 vol.% GNP content-reinforced  $\text{Al}_2\text{O}_3$  nanocomposites had significantly improved flexural strength and fracture toughness by approximately 60% and 70%, respectively. Ahmad et al. [1] studied the influence of multi-layer graphene (MLG) contents (0.5 vol.% and 1.00 vol.%) on the density, hardness, structural, wear resistance, and tribological properties of fabricated nanocomposites using an HFIHS. The results showed that the nanocomposites with 1 vol.%

MLGs exhibited 15% and 25% lower friction coefficients than the nanocomposites with 0.5 vol.% MLGs and monolithic Al<sub>2</sub>O<sub>3</sub>, respectively. Ahmad et al. [30] studied the effect of adding GNPs on the thermophysical properties of fabricated GNP/Al<sub>2</sub>O<sub>3</sub> nanocomposites using HFIH. The obtained results showed that the nanocomposites with 0.5 wt.% GNP content exhibited hardness and fracture toughness values of 18.4 GPa and 5.7 Joule/m, respectively, which were higher than those of monolithic Al<sub>2</sub>O<sub>3</sub>. Moreover, the Al<sub>2</sub>O<sub>3</sub> showed the highest thermal conductivity value. Shah et al. [11] studied the effects of graphene content (0 wt.%, 0.4 wt.%, 0.8 wt.%, 1.2 wt.%, and 1.6 wt.%) on the density, microstructure, fracture toughness hardness, and strength of graphene-reinforced Al<sub>2</sub>O<sub>3</sub> nanocomposites. The nanocomposite samples were prepared by ultra-sonication and the SPS process. The results showed that the density and bending strength slightly decreased with increasing graphene content from 0.4 wt.% to 1.2 wt.%. Moreover, all the nanocomposites revealed improved fracture toughness compared to the monolithic Al<sub>2</sub>O<sub>3</sub> samples. Table 1 summarizes some of the works reported on the preparation, characterization, and machining of Al<sub>2</sub>O<sub>3</sub> nanocomposites reinforced with graphene.

**Table 1.** The fabrication techniques of graphene-reinforced alumina ceramic nanocomposites presented in the literature.

Ref.	CMC	Reinforcement Ratio	Preparation Method	Consolidation Method	Studied Characteristics	Machining Analysis
[31]	GNS/Al <sub>2</sub> O <sub>3</sub>	3, 3.5, 4, 5, 10 and 15 vol.%	Dry ball milling	SPS	Electrical conductivity	No
[25]	GNS/Al <sub>2</sub> O <sub>3</sub>	0.2, 0.5, 0.8, 2 and 5 vol.%	Wet ball milling	SPS	Fracture toughness and elastic modulus	No
[26]	GNS/Al <sub>2</sub> O <sub>3</sub>	0.1, 0.2, 0.5, and 1 wt.%	Wet ball milling	HP	Microstructure and fracture toughness	No
[32]	GNP/Al <sub>2</sub> O <sub>3</sub>	0.5, 2, and 5 vol.%	Wet ball milling	SPS	Scratch testing	No
[33]	GNP/Al <sub>2</sub> O <sub>3</sub> CNT/Al <sub>2</sub> O <sub>3</sub>	1, 2 wt.%	Ultrasonic probe	HP and SPS	Morphology, grain sizes, and fracture mode	No
[10]	GNS/Al <sub>2</sub> O <sub>3</sub>	0.25, 0.5, 1.5, 3 wt.%	Ultrasonic probe	HFIHS	Hardness, elastic modulus, and fracture toughness	No
[34]	GNP/Al <sub>2</sub> O <sub>3</sub>	5, 10, 15, 20 vol.%	Wet ball milling	SPS	Hardness and electrical conductivity	Yes
[29]	GNP/Al <sub>2</sub> O <sub>3</sub>	0.75, 1.17, 1.85, and 2.75 vol.%	Wet ball milling	Pressure-less sintering	Hardness, flexural strength, fracture toughness, and biocompatibility	No
[35]	GNP/Al <sub>2</sub> O <sub>3</sub>	5, 10, 15 vol.%	Wet ball milling	SPS	Fracture toughness, wear resistance, and biocompatibility	No
[30]	MLG/Al <sub>2</sub> O <sub>3</sub>	0.5, 1.0 vol.%	Aqueous sonic probe	HFIHS	Wear-resistance properties	No
[13]	MLG/Al <sub>2</sub> O <sub>3</sub>	0.2, 0.5, 0.7, and 1 wt.%	Wet ball milling	SPS	Microstructure and tribological performance	No

Graphene-based alumina matrix nanocomposites

As is evident in the literature, adding graphene-based reinforcements has a great impact on the physical and mechanical properties of Al<sub>2</sub>O<sub>3</sub>. Therefore, there is immense potential in exploring their machining behavior. Several studies have been reported in the literature regarding the machining of pure Al<sub>2</sub>O<sub>3</sub> ceramic [36,37], but studies related to the machining of graphene-based alumina nanocomposites are scarce. As shown in Table 1, only Sung et al. [38] investigated the electrical discharge machining (EDM) of the graphene-reinforced Al<sub>2</sub>O<sub>3</sub> nanocomposites, while the remaining studies only focused on their characterization. Sung et al. [38] reported that an increase in the electrical conductivity of the graphene-reinforced Al<sub>2</sub>O<sub>3</sub> nanocomposites led to significant improvement in their EDM. Moreover, they found that an increase in the surface roughness was observed at the high graphene content of 15 wt.%.

No detailed work has been presented so far on the effect of graphene reinforcement on the machining behavior of these new materials. Only a study reported by Lee et al. [38] explored the effect of GNPs and CNT on optical absorbance and thermal conductivity. They found that the optical absorbance and thermal conductivity of nanocomposites were improved compared to pure alumina. To utilize graphene-reinforced  $\text{Al}_2\text{O}_3$ -based nanocomposites in various applications, it is essential to study their machinability in detail. Therefore, this study aimed to develop a detailed understanding of the effect of graphene reinforcement to improve the microfabrication performance of  $\text{Al}_2\text{O}_3$ -based nanocomposites to satisfy sustainable manufacturing requirements. To achieve this aim, high-density  $\text{Al}_2\text{O}_3$  nanocomposite samples were produced with different graphene contents using dry ball-milling and HFIHS techniques. The density, hardness, and microstructure were studied to evaluate the nanocomposite specimens. After that, detailed micromachining experiments were conducted to study the effect of the GNP contents and machining parameters on the microfabrication performance of  $\text{Al}_2\text{O}_3$ -based nanocomposites. The surface integrity, surface roughness, ablation depth, and material removal rate were used to compare the microfabrication performance of the developed GNP/ $\text{Al}_2\text{O}_3$  nanocomposites.

## 2. Experimental Procedure

### 2.1. Fabrication of Nanocomposites

Commercial alumina powder with a particle size of 300 nm was used as the matrix material, supplied by US Research Nanomaterials, Inc. (Houston, TX, USA). The chemical composition of the received alumina powder is provided in Table 2. Figure 1a shows the morphology of the received  $\text{Al}_2\text{O}_3$  powder.

**Table 2.** Composition of alumina powder.

Elements	$\text{Al}_2\text{O}_3$	$\text{B}_2\text{O}_3$	CaO	$\text{Fe}_2\text{O}_3$	MgO	$\text{Na}_2\text{O}$
Percentage (wt.%)	$\geq 99.9$	$\leq 0.002$	$\leq 0.01$	$\leq 0.01$	$\leq 0.02$	$\leq 0.03$

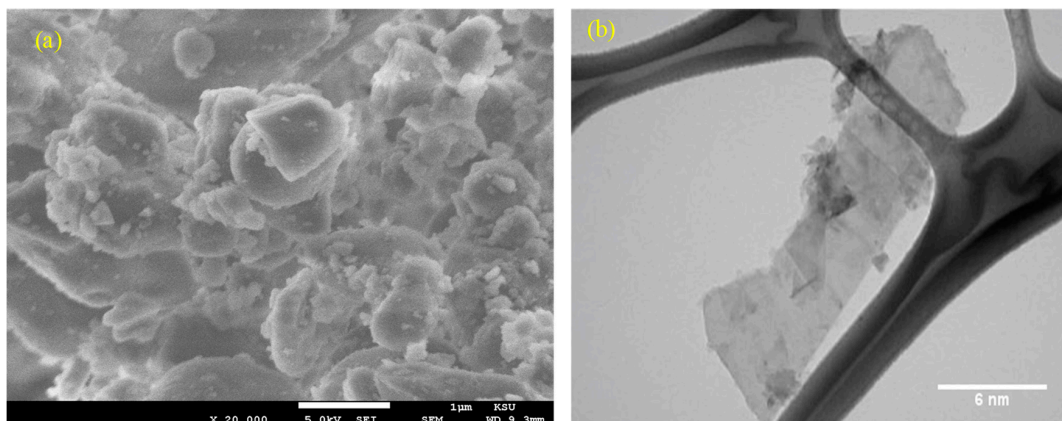


**Figure 1.** Morphology of the received powder. (a)  $\text{Al}_2\text{O}_3$  and GNPs; (b) GNPs (XG Sciences, Inc., USA).

Graphene nanoplatelets (GNPs), supplied by XG Sciences, Inc. (Lansing, MI, USA), were used as the reinforcement material. The characteristics of the GNPs are listed in Table 3. The morphology of the received GNP powder is shown in Figure 1b.

**Table 3.** Characteristics of GNPs.

Powder	Average Diameter	Thickness	Surface Area	Density
GNPs	Less than 2 $\mu\text{m}$	5–8 nm	750 $\text{m}^2/\text{g}$	2.21 $\text{g}/\text{cm}^3$

To fabricate the GNP-reinforced  $\text{Al}_2\text{O}_3$  nanocomposites, the initial powder mixing was a critical step in ensuring the homogenous dispersion of the GNPs in the base  $\text{Al}_2\text{O}_3$

powder. Several techniques mentioned in Table 1 are used for powder mixing. In this work, the planetary ball-milling technique was used to prepare the nanocomposites. All the powders (with or without GNPs) were mechanically ball-milled using the Pulverisette machine (FRITSCH GmbH, Idar-Oberstein, Germany). The GNP/ $\text{Al}_2\text{O}_3$  nanocomposites were prepared using different weight percentages of reinforcement, including 0 wt.% (base  $\text{Al}_2\text{O}_3$ ), 0.5 wt.%, 1 wt.%, 1.5 wt.%, and 2.5 wt.% GNPs. The GNP weight percentages were selected based on the preliminary experiments, which demonstrated that using a GNP wt.% of  $>2.5$  led to compromised mechanical properties. The ball-milling was performed in cylindrical zirconia containers using yttria-stabilized zirconia balls (diameter = 15 mm) at 350 rpm for 4 h under a ball-to-powder weight ratio of 20:1 [39]. A schematic diagram of the ball-milling process of GNP-reinforced nanocomposites is illustrated in Figure 2a. The ball-milled powder was loaded into a graphite die with an internal diameter of 20 mm and then consolidated by an HFIHS furnace (HF Active Sinter System, ELTek CO., Gyeonggi-do, Republic of Korea), as shown in Figure 2b, at a temperature of 1500 °C, a heating rate of 150 °C/min, uniaxial pressure of 60 MPa, and a cooling rate of 200 °C/min in a vacuum (45-Torr) [10,30]. The dimensions of the fabricated specimens were 20 mm in diameter and 12 mm in height.

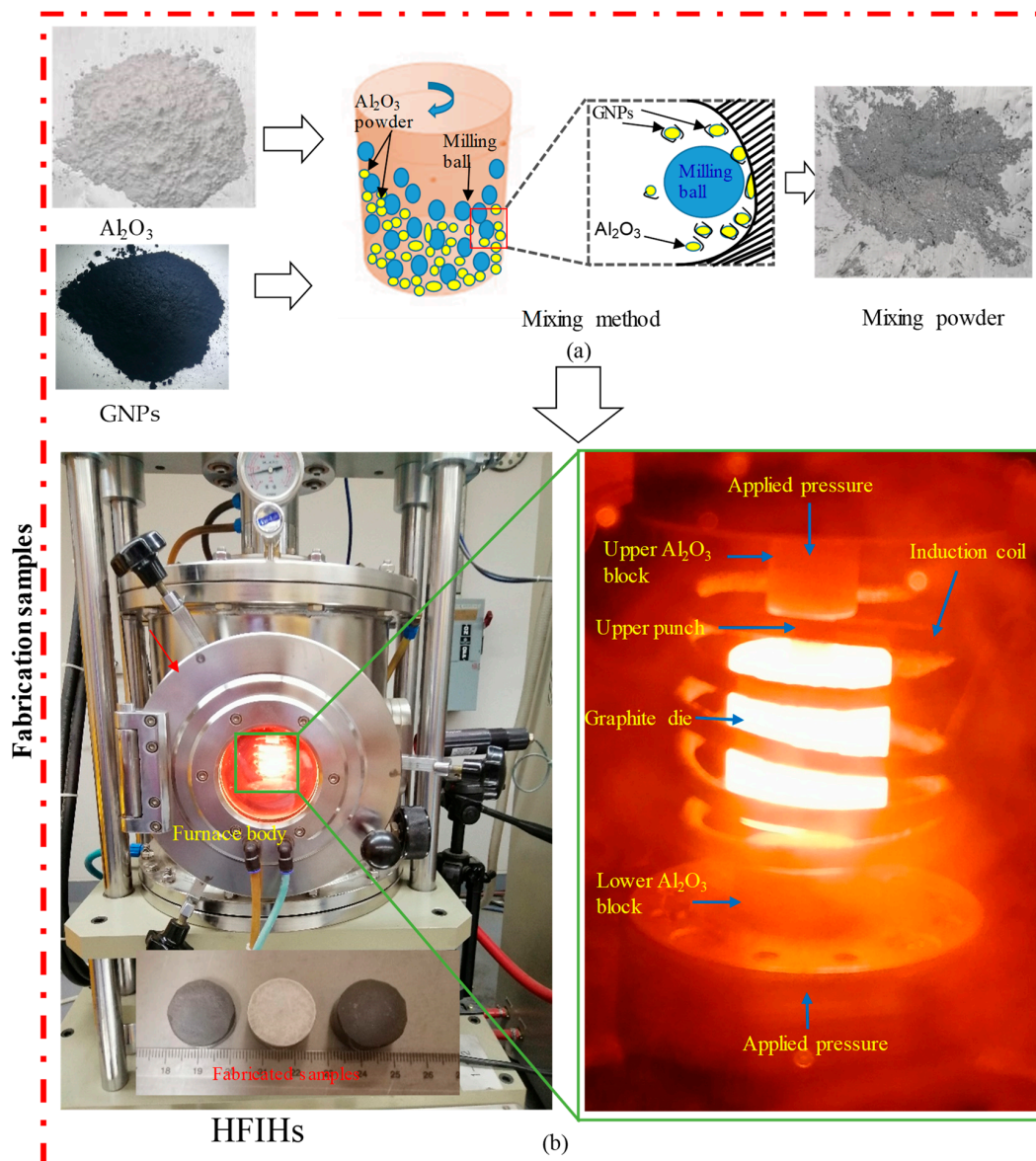


Figure 2. Experimental setup for fabricating the GNP/ $\text{Al}_2\text{O}_3$  specimens.

## 2.2. Machining and Measurements Setups

Laser microfabrication experiments were performed on the GNP/ $\text{Al}_2\text{O}_3$  nanocomposites using an XTL-FP 20 laser machine from XT laser, Jinan, China, as shown in Figure 3a. This fiber laser requires very low power consumption (20 W). The laser beam was focused using a flat-field lens, moved through a galvanometric mirror system, and irradiated on the top surface of the fabricated GNP/ $\text{Al}_2\text{O}_3$  specimens. Figure 3b shows a schematic diagram of laser beam machining. These types of laser sources have been designed specifically for the marking/engraving of metallic materials, such as steel and aluminum. In addition, they are adopted for different applications, such as surface treatments and micromachining operations. However, in this work, this low-power and low-cost laser machine was adapted for testing the machinability of the GNP/ $\text{Al}_2\text{O}_3$  ceramic nanocomposites. It is worth mentioning that pure  $\text{Al}_2\text{O}_3$  ceramic is extremely difficult to machine even with sophisticated high-power laser machines, such as that reported by [40]. Poor machining in terms of the microchannel shape and dimensions and the surface integrity have been reported even using expensive laser setups [40,41]. In this paper, it is shown that the addition of GNPs in  $\text{Al}_2\text{O}_3$  enabled high-quality laser machining even with a very low cost, low power (20 W), and an easily accessible laser machine (XTL-FP 20 laser). This meets the requirements of clean, sustainable manufacturing where high-quality products (e.g., microchannels) can be produced with lower costs and resources.

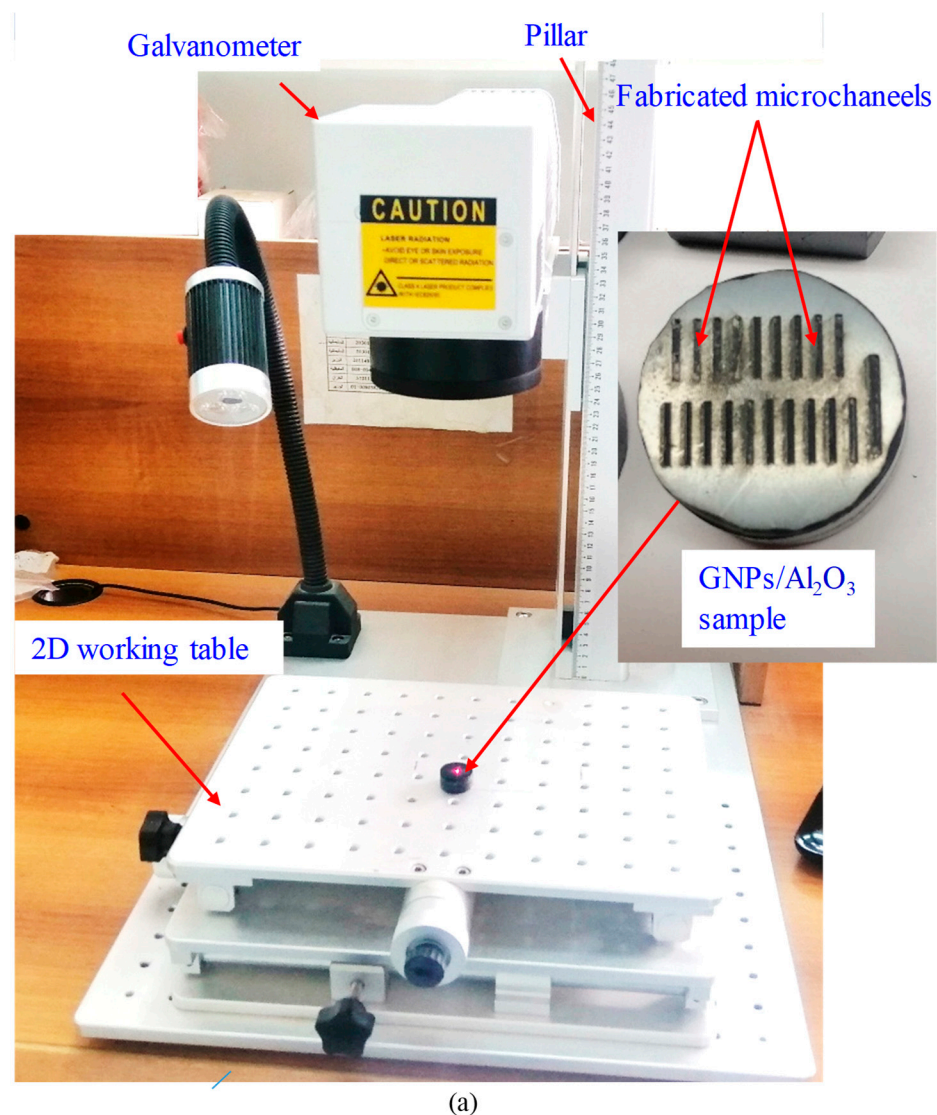
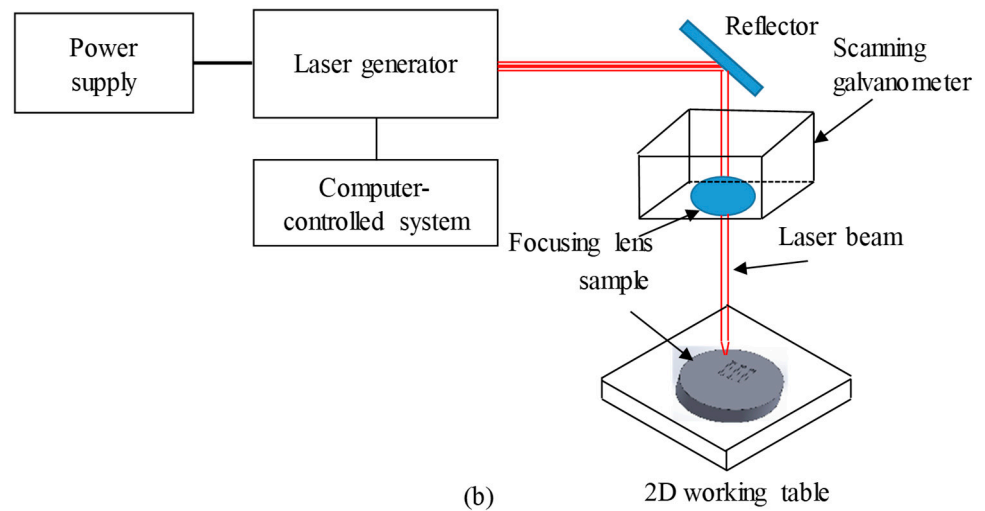


Figure 3. Cont.



**Figure 3.** (a) Laser beam machining setup; (b) schematic diagram of laser beam machining.

Microchannels with the dimensions of 250  $\mu\text{m}$  in width and 5 mm in length were fabricated on all produced GNP/ $\text{Al}_2\text{O}_3$  nanocomposites with varying GNP contents. Before the main experiments, all fabricated samples were ground to remove the superficial graphite and oxide layers and non-uniformity. Later, two laser parameters, i.e., the scanning speed and pulse frequency, were varied during the laser micro-milling. There is no information available in the literature regarding the laser micromachining of GNP/ $\text{Al}_2\text{O}_3$  matrix nanocomposites. Therefore, initially, preliminary tests were conducted to identify the suitable ranges of influential factors using the reported studies on the micromachining of alumina ceramics [40,42,43]. Table 4 shows the selected laser parameters and their ranges.

**Table 4.** Laser parameters and their selected ranges.

Input Parameters	Values			
Scanning speed, SS (mm/s)	200	300	400	500
Pulse frequency, F (kHz)	20	30	40	-
Power, (w)	20	-	-	-
Scanning strategy	Line	-	-	-
Line spacing	17 $\mu\text{m}$	-	-	-
Spot diameter	50 $\mu\text{m}$	-	-	-
Pulse overlap	50%	-	-	-
Step overlap	5%	-	-	-

Parameters such as the power (20 W), scanning strategy (line strategy), and line spacing were kept constant throughout all the tests, as shown in Figure 4. In addition, to evaluate the effects of graphene content on the fabrication of microchannels, five specimens with 0.0 wt.%, 0.5 wt.%, 1 wt.%, 1.5 wt.%, and 2.5 wt.% GNPs were machined with the same laser parameters. Each test was repeated three times for each microchannel to guarantee the repeatability of the experiments, and later, the average value was used. The output responses, including the microchannels' geometries (depth and top width), material removal rate, surface roughness, and surface morphology, were used to appraise the influence of the graphene contents on the micromachining behavior of the GNP/ $\text{Al}_2\text{O}_3$  nanocomposites. After machining, all machined specimens were first cleaned using ethanol to remove any loose debris or contaminants on the fabricated microchannels [44]. Then, the dimensional accuracy and surface roughness were measured by a 3D optical profilometer (DektakXT Stylus Profiler) from Bruker (Billerica, MA, USA). The optical 3D profilometer was equipped with an inductive gauge of 12.5  $\mu\text{m}$  radius diamond stylus, as shown in Figure 5a. The ablated depth and width were measured by capturing four random 2D profiles along the width of the fabricated channels with a scanning speed of 5  $\mu\text{m}/\text{s}$  (see

Figure 5c). The average of the measured values was used later to measure the dimensional accuracy (depth and width). The roughness was measured in terms of the arithmetic mean surface roughness ( $Ra$ ) according to the ISO 4287 standard. The surface roughness was measured by scanning four random measurements along the bottom length of the channels, and averaged values were used for further analysis (see Figure 5b). The surface morphologies of the machined microchannels were analyzed using a scanning electron microscope (SEM) from Jeol Japan (Model JCM 6000 Plus). Before capturing the SEM images, a platinum coating was applied to all machined samples using the JFC 1600 auto fine coater (JEOL Ltd., Tokyo, Japan) to enhance their visibility. The material removal rate (MRR) was used to assess the effect of the graphene contents on the laser micromachining of the nanocomposites. The MRR was calculated using Equation (1).

$$MRR = \frac{\text{Machined area} \times \text{machined length}}{\text{machining time}} \quad (\text{mm}^3/\text{min}) \quad (1)$$

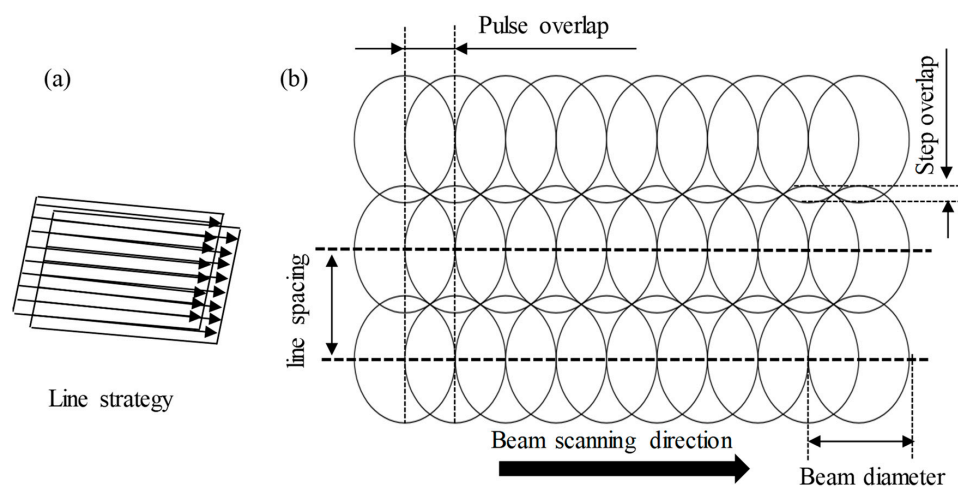


Figure 4. (a) Laser scanning strategy; (b) schematic of the adjacent laser tracks.

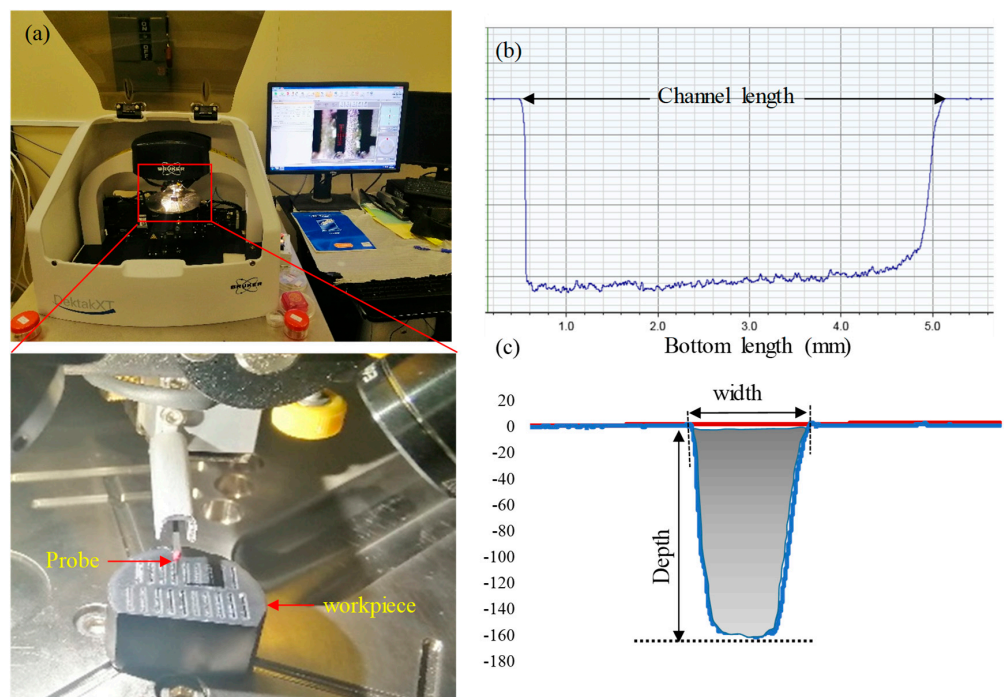


Figure 5. Measuring devices. (a) Three-dimensional optical profilometer; (b,c) typical geometry of the 2D profile and its cross-sectional area.

The cross-section of the machined area was calculated from the fitted 2D profile, as shown by the grey-filled area in Figure 5c. The cross-sectional area of the four profiles was averaged and then used in Equation (1).

### 3. Results and Discussions

#### 3.1. Characterization of the Fabricated GNP/Al<sub>2</sub>O<sub>3</sub>-Based Nanocomposites

##### 3.1.1. Microstructure Evaluation

Figure 6 shows the morphologies of the fractured surfaces for the base Al<sub>2</sub>O<sub>3</sub> and the GNP/Al<sub>2</sub>O<sub>3</sub> nanocomposites. It can be seen that the GNP/Al<sub>2</sub>O<sub>3</sub> nanocomposites had a smaller grain size compared to the base Al<sub>2</sub>O<sub>3</sub>. The addition of the GNPs tended to restrict grain growth by acting as an obstruction between the Al<sub>2</sub>O<sub>3</sub> matrix particles.

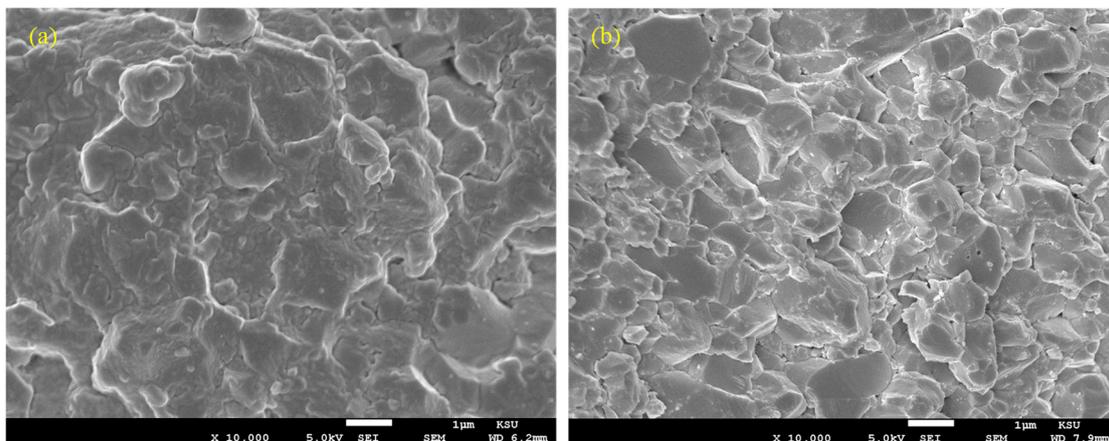


Figure 6. SEM images showing the fractured surfaces of (a) base Al<sub>2</sub>O<sub>3</sub>; (b) 1.5 wt.% GNP/Al<sub>2</sub>O<sub>3</sub>.

##### 3.1.2. Density Analysis

The actual density of the fabricated GNP/Al<sub>2</sub>O<sub>3</sub> nanocomposites was measured using the Archimedes method by employing the density measurement system from Sartorius Lab Instruments, Goettingen, Germany. Afterward, the relative density was calculated by dividing the actual density by the theoretical density [45] of the powder mixture, as shown in Figure 7. It can be seen in Figure 7 that the fabricated GNP-reinforced Al<sub>2</sub>O<sub>3</sub> nanocomposite samples exhibited a high relative density, which indicates good bonding between the GNPs and the Al<sub>2</sub>O<sub>3</sub> matrix, with negligible porosity or cavities.

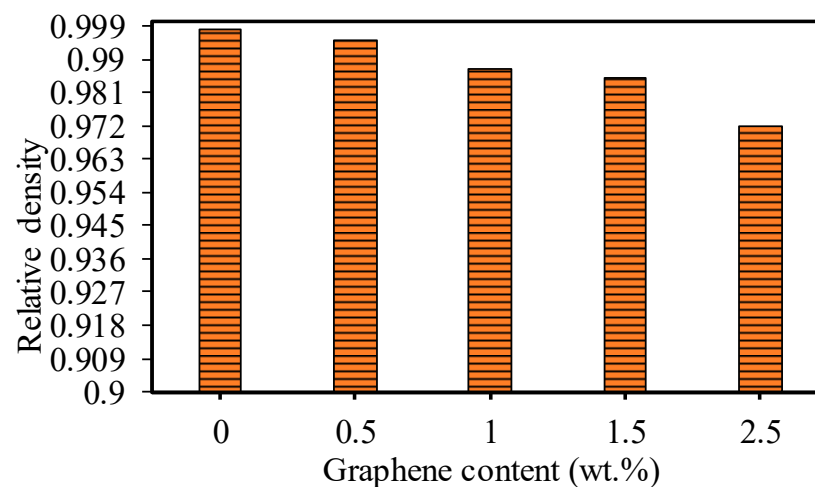
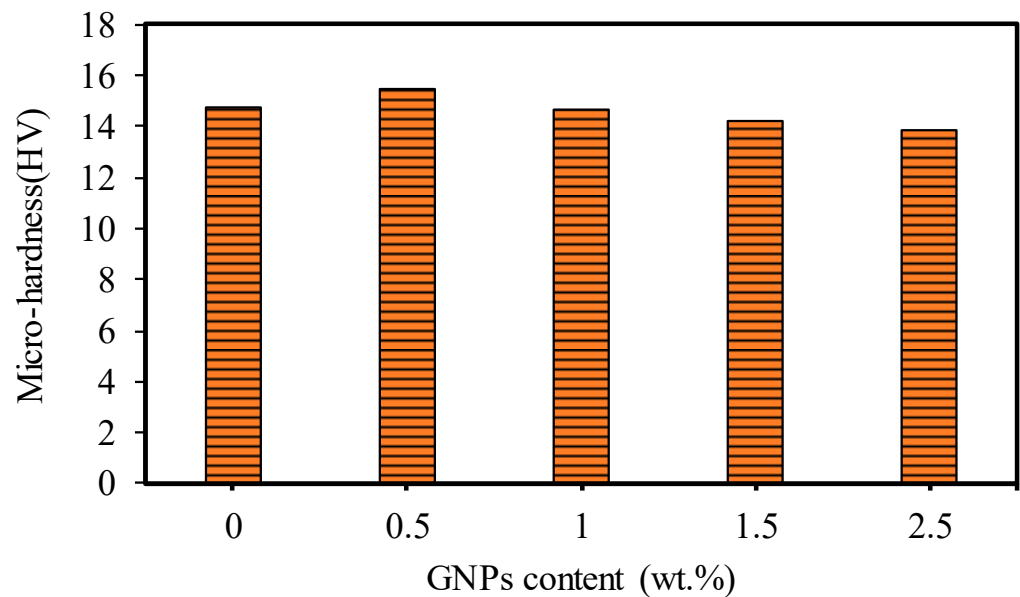


Figure 7. Relative density of the base Al<sub>2</sub>O<sub>3</sub> and GNP/Al<sub>2</sub>O<sub>3</sub> nanocomposites with different GNP contents.

### 3.1.3. Hardness

The ZHV30 Vickers Hardness Tester was used to measure the Vickers hardness of the fabricated specimens using a load of 30 kg for a dwell time of 12 s. For each specimen, the hardness measurement was repeated six times at different locations on the ground surface, and later, the average value was used, as shown in Figure 8. It can be seen that nanocomposites with 0.5 wt.% GNPs had the highest hardness by approximately 7% compared to the base  $\text{Al}_2\text{O}_3$ . This can be attributed to the presence of GNPs among the  $\text{Al}_2\text{O}_3$  particles, inhibiting grain growth and resulting in a smaller grain size and good interfacial bonding between the  $\text{Al}_2\text{O}_3$  particles [10,16]. With GNP contents of 1 wt.% and 1.5 wt.%, the Vickers hardness slightly decreased. This can be attributed to the presence of the thicker layer of GNPs among the  $\text{Al}_2\text{O}_3$  grains, which led to a weakening of the interfacial bonding between the  $\text{Al}_2\text{O}_3$  particles and reduced hardness [1,10,16].



**Figure 8.** Hardness for the base  $\text{Al}_2\text{O}_3$  and GNP/ $\text{Al}_2\text{O}_3$  nanocomposites.

## 3.2. Micromachining Results and Discussion

### 3.2.1. Surface Morphology

Figures 9–12 show the surface morphologies of the laser-fabricated microchannels on the base  $\text{Al}_2\text{O}_3$  and GNP/ $\text{Al}_2\text{O}_3$  nanocomposites at lower (200 mm/s) and higher (500 mm/s) scan speeds. The results show that the microchannels of the GNP/ $\text{Al}_2\text{O}_3$  nanocomposites had overall better surface quality and geometry compared to the base  $\text{Al}_2\text{O}_3$  specimens in all machining conditions. This is because of the presence of the GNPs among the  $\text{Al}_2\text{O}_3$  matrix particles, which enhanced the thermal conductivity and optical absorbance properties during the laser micromachining. These properties induced higher surface melting and evaporation at even lower energy densities. Kim et al. [46] found that the presence of CNT enhanced the machinability of CNT/Fe/ $\text{Al}_2\text{O}_3$  nanocomposites due to the addition of the CNT, which led to lower light transmittance, higher thermal conductivity, and suppressed grain growth.

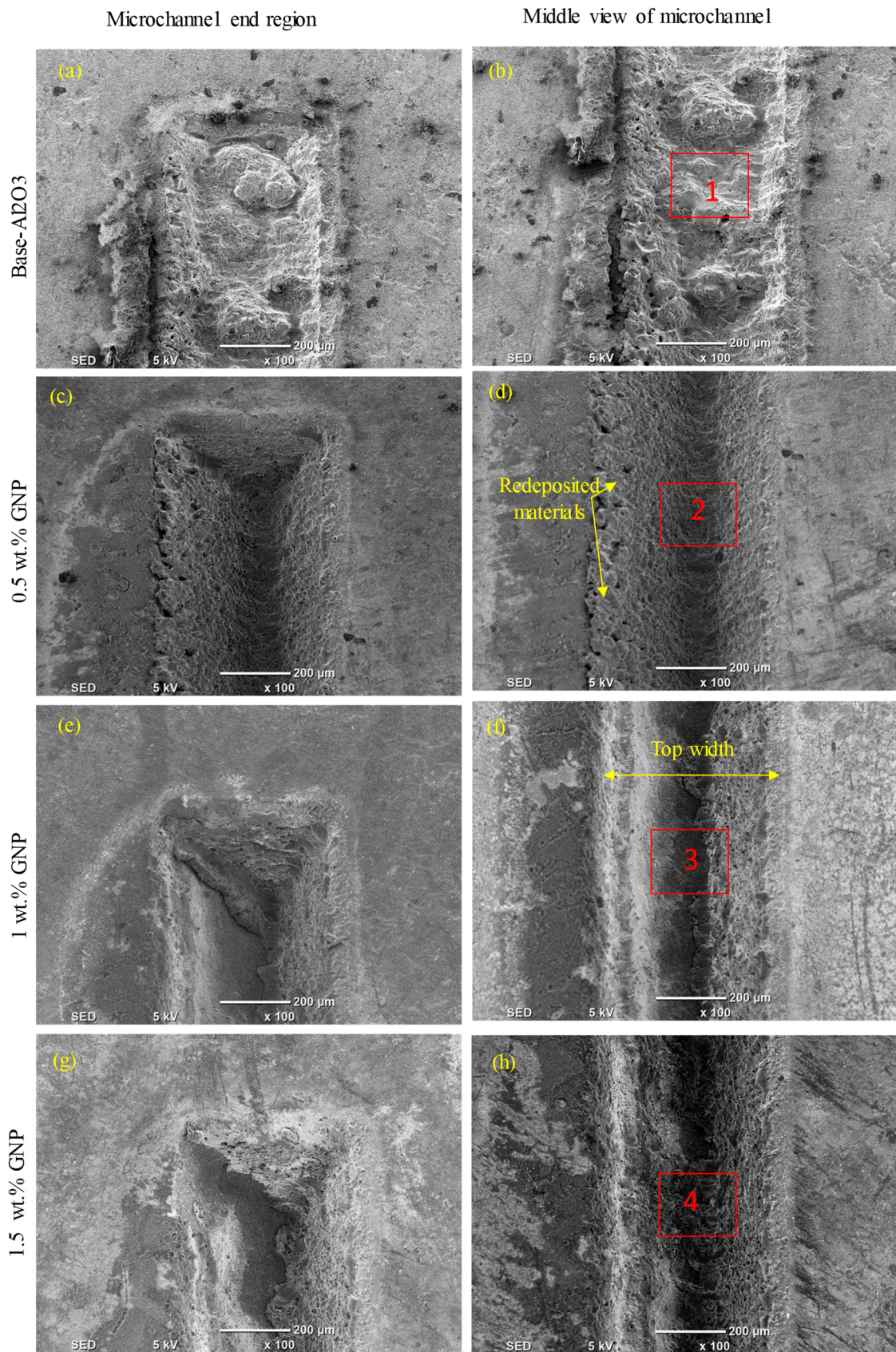
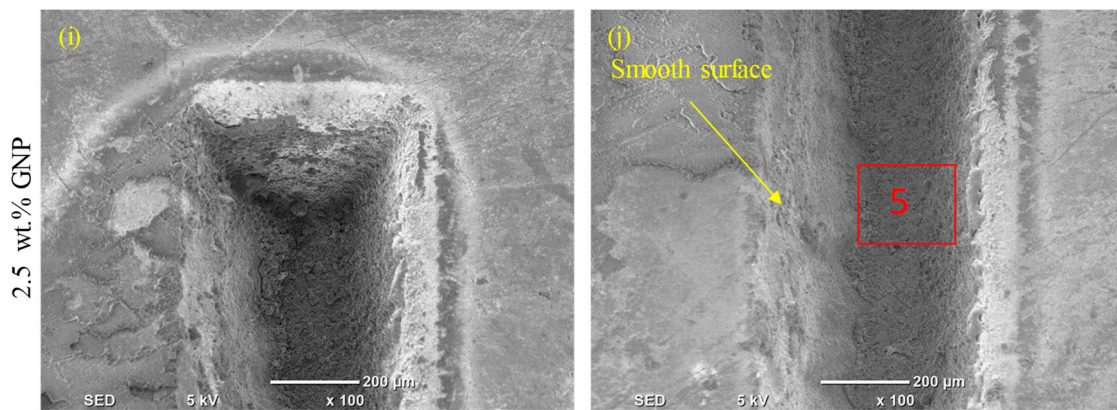
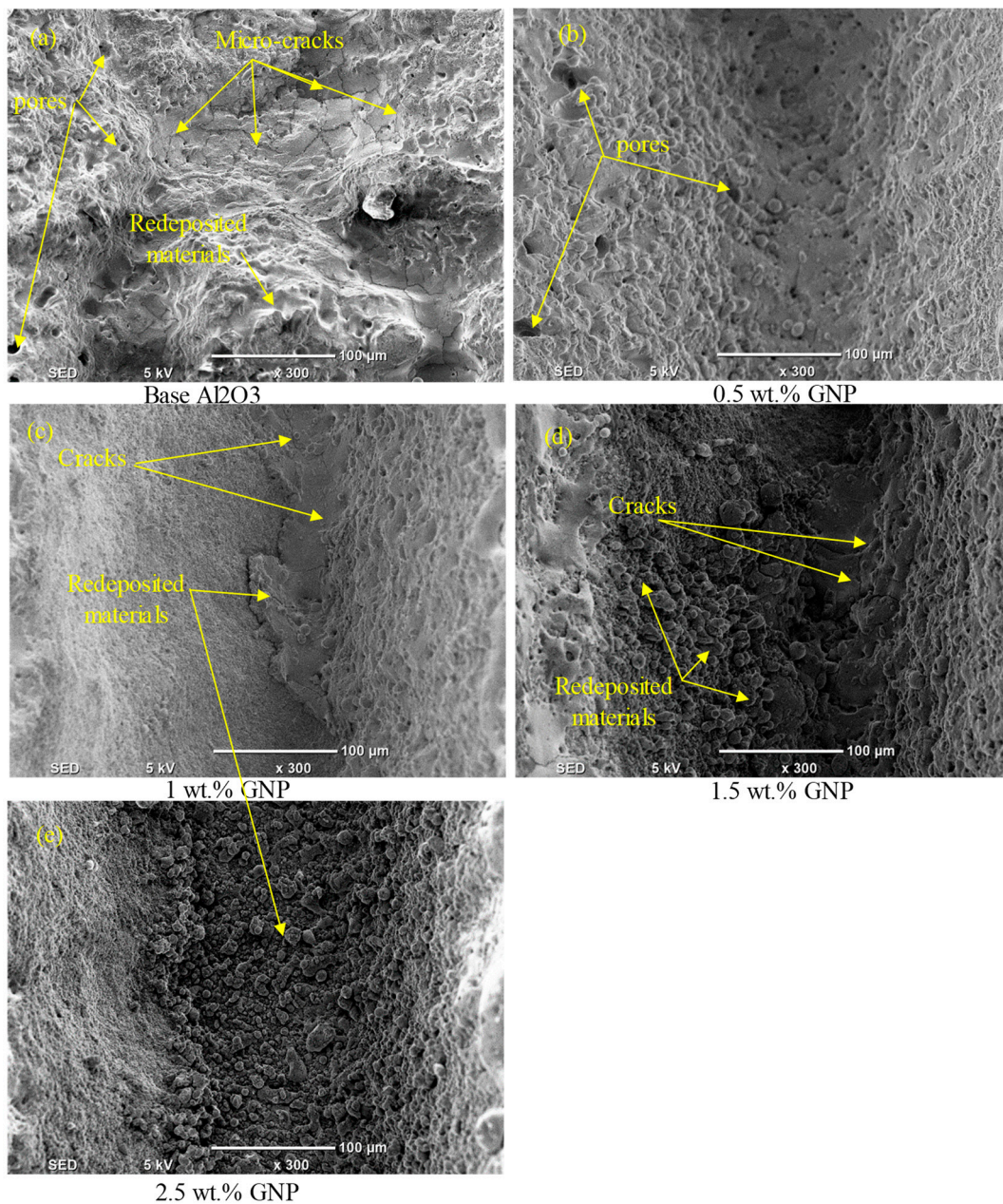


Figure 9. Cont.



**Figure 9.** Surface morphology of the ablated base  $\text{Al}_2\text{O}_3$  and GNP/ $\text{Al}_2\text{O}_3$  nanocomposites with varying graphene contents at 200 mm/s.



**Figure 10.** Zoomed-in images of the selected regions (1–5) shown in Figure 9.

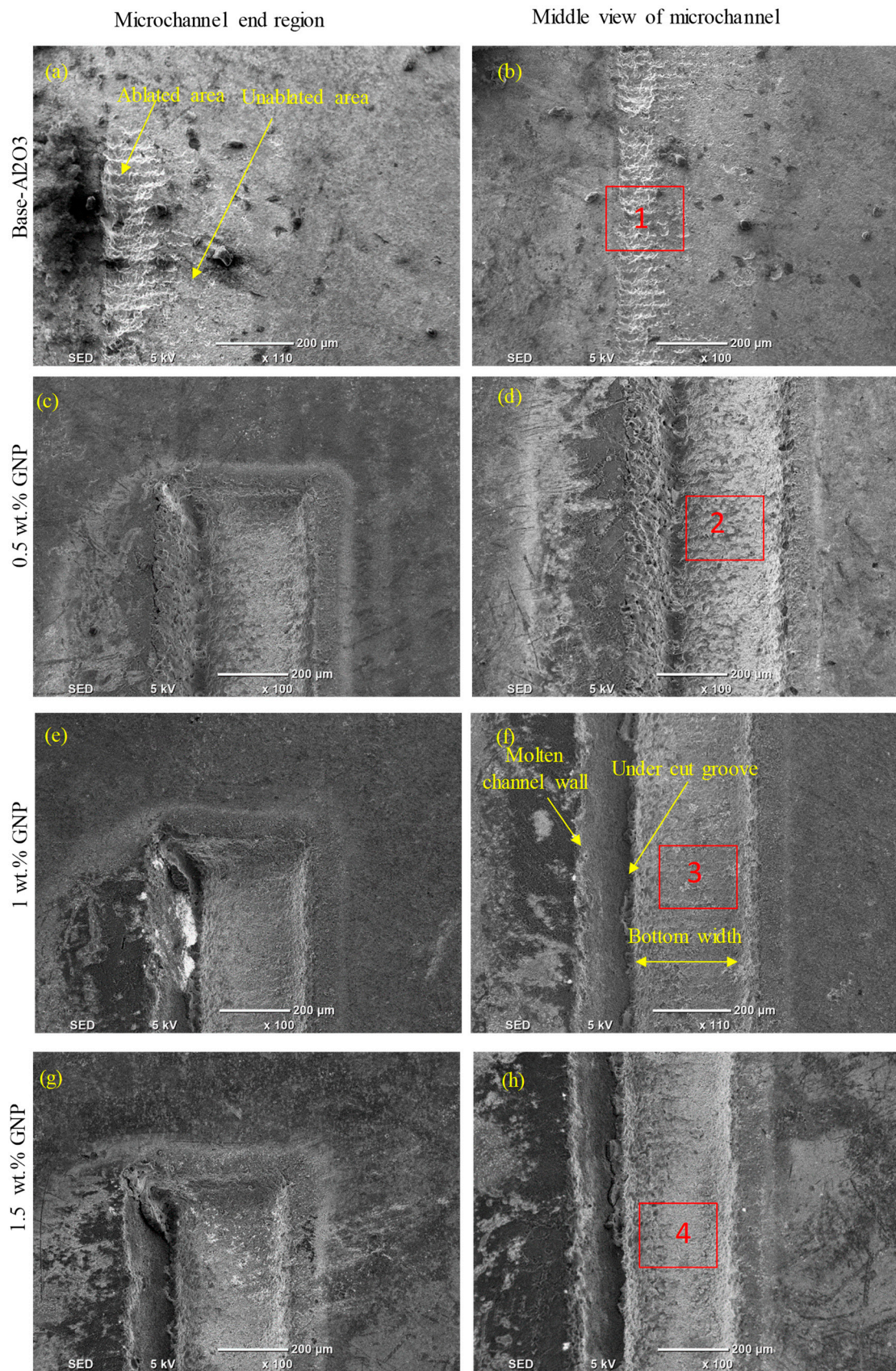


Figure 11. Cont.

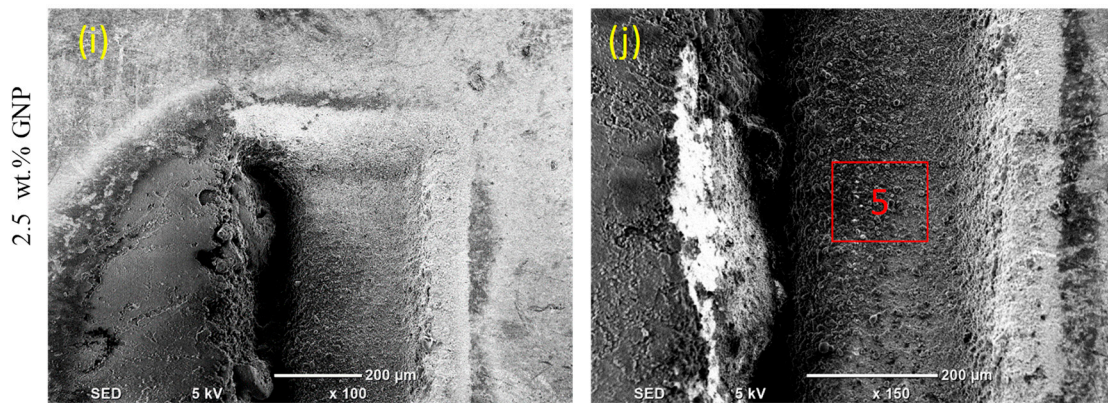


Figure 11. Surface morphologies of the ablated base  $\text{Al}_2\text{O}_3$  and GNP/ $\text{Al}_2\text{O}_3$  nanocomposites with varying graphene contents at 500 mm/s.

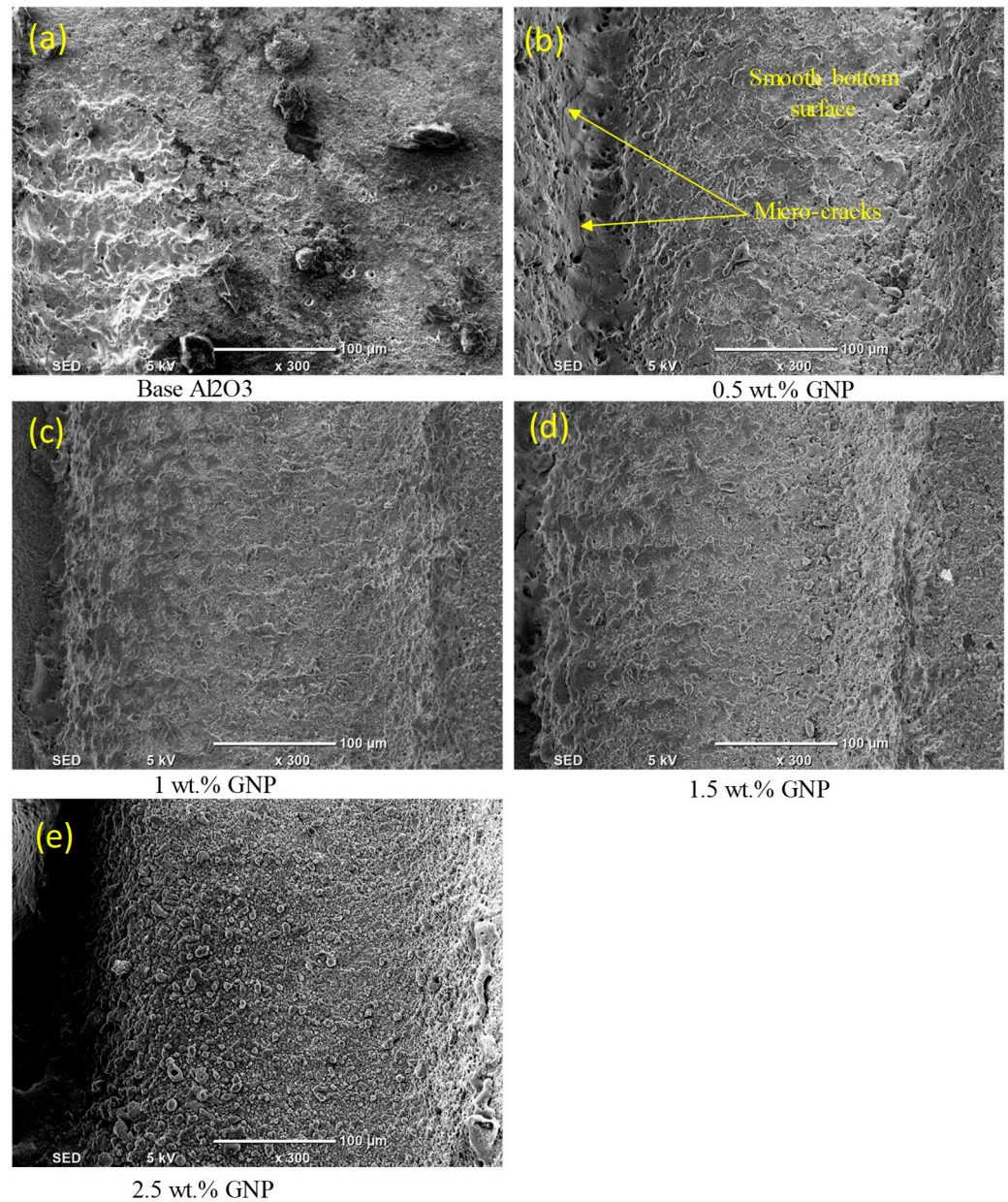


Figure 12. Zoomed-in images of the selected regions (1–5) shown in Figure 11.

At a scan speed of 200 mm/s (see Figure 9), it can be seen that redeposited material, cracks, and pores were formed on the bottom surface of the microchannel and on the surrounding sidewalls in the case of the base  $\text{Al}_2\text{O}_3$ , as shown in Figures 9a,b and 10a. On the contrary, a much more regular and smoother channel was observed for the nanocomposites with 0.5 wt.% GNPs at a scan speed of 200 mm/s, as can be seen in Figures 9c,d and 10b. The surface morphology of the ablated microchannels shows a higher ablation with few cracks and pores on the bottom and sidewalls of the microchannels (see Figures 9c,d and 10b). This can be attributed to the higher energy absorption of the nanocomposites, which required less energy for melting the surfaces of the specimens. For the 1 wt.% GNP specimens, the fabricated microchannels on the nanocomposites had visible and irregular redeposited materials and microcracks on the bottom surface at a scanning speed of 200 mm/s. In addition, the sidewalls of the microchannels became smoother with a marginal recast layer compared to the specimens with a 0.5 wt.% GNP content (see Figures 9e,f and 10c). This was due to the increase in the GNP contents, which increased the optical absorbance of the specimens, causing more melting materials compared to the 0.5 wt.% GNP specimens. On the contrary, for the 1.5 wt.% GNP/ $\text{Al}_2\text{O}_3$  nanocomposite, the surface morphology of the fabricated channel had a rough surface at a lower scanning speed of 200 mm/s compared to the 0.5 wt.% and 1 wt.% GNP specimens (see Figures 9g,h and 10d). This was because of the lower ablation threshold energy for the 1 wt.% GNP specimens, which induced more melting material compared to the lower GNPs content. In addition, the increase in the GNP content resulted in an increase in the material's thermal conductivity, which allowed the molten material at the bottom and sides of the microchannels to resolidify faster. This was observed as thicker re-solidified layers, microcracks, and pores around the side wall, and rougher bottom surfaces of the microchannels as the GNP wt.% increased. For the same reasons, the nanocomposites with 2.5 wt.% GNPs exhibited the worst surface morphology, with more redeposited material and pores compared to the 0.5 wt.%, 1 wt.%, and 1.5 wt.% GNP specimens, as shown in Figures 9i,j and 10e.

At a high scanning speed of 500 mm/s, it was evident that no well-defined microchannels were created; instead, only multiple-pulse traces of the laser beam were seen on the base  $\text{Al}_2\text{O}_3$  specimens. The base  $\text{Al}_2\text{O}_3$  presented poor laser machinability compared to all of the GNP/ $\text{Al}_2\text{O}_3$  nanocomposites, as shown in Figures 11a,b and 12a. The laser-ablated nanocomposites with 0.5 wt.% GNPs showed well-defined microchannels. In addition, the ablated depths of the microchannels decreased, and some cracks, pores, and redeposited materials on the bottoms of the channels were formed, resulting in an increase in the surface roughness (see Figures 11c,d and 12b). Moreover, it can be seen in the SEM images that the microchannel shape changed from triangular to trapezoidal with the increase in the scanning speed from 200 mm/s to 500 mm/s (compare Figures 9c and 11c). For the 1 wt.%, 1.5 wt.%, and 2.5 wt.% GNP specimens, smoother surface morphologies were noted at 500 m/s compared to the 0.5 wt.% GNP specimens (see Figures 11e–j and 12c–e), contrary to the scanning speed at 200 mm/s. This is because at a higher scanning speed (500 mm/s), the laser–workpiece interaction time was reduced, and samples with a higher ablation threshold (0.5 wt.% GNPs) were not adequately irradiated to melting and evaporation. As the GNP contents increased, the optical absorbance of the specimens increased, resulting in more molten and evaporated material from the walls and bottoms of the channels compared to the 0.5 wt.% GNP specimens (Figures 11i,j and 12e).

### 3.2.2. Microchannel Accuracy

Figure 13a,b shows the effect of the GNP contents with varying scanning speeds on the channel depth and width. It can be concluded from Figure 13a that the channel depth increased with an increment in the GNP percentage from 0.0 wt.% to 2.5 wt.%. This is attributed to the improved thermal conductivity and optical absorbance of the GNP/ $\text{Al}_2\text{O}_3$  nanocomposites, as discussed in Section 3.2.1 [31,39,47], leading to lowering the ablation threshold of the composites due to the addition of the GNPs. Therefore, the channel depth increased for the GNP/ $\text{Al}_2\text{O}_3$  nanocomposites by around two to nine times compared to

the base  $\text{Al}_2\text{O}_3$ . In addition, the channel depth increased with the increasing graphene contents from 0.5 wt.% to 2.5 wt.% due to further increases in the thermal conductivity, optical absorbance, and reduced grain size [48].

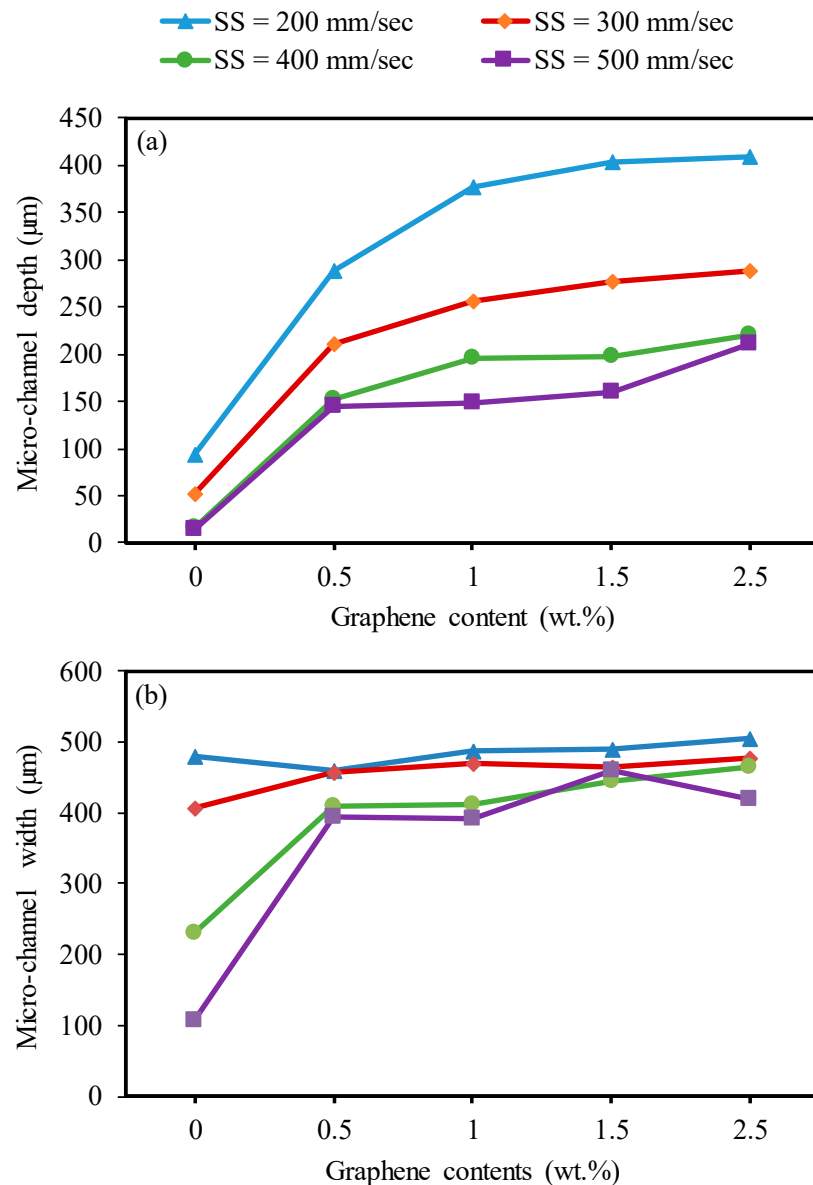


**Figure 13.** Effects of varying graphene reinforcement contents with laser speed on microchannel depth and width for machining base  $\text{Al}_2\text{O}_3$ , and GNP/ $\text{Al}_2\text{O}_3$  nanocomposites at  $F = 30$  kHz. (a) Microchannel depth, (b) Microchannel width.

At a higher scanning speed of 500 mm/s, the channel depth tended to decrease slightly with the GNP content rising from 1 wt.% to 1.5 wt.%, and then increased with the GNP content rising to 2.5 wt.%. The main reason for the improvement in the microchannel depth is shown in Figure 14. When the graphene content increased from 0.0 wt.% to 0.5 wt.%, more material melted, and less material was redeposited on the microchannel bed. Hence, the microchannel depth increased (see Figure 14b). When the graphene content increased from 0.5 wt.% to 1 wt.%, the microchannel depth increased because more induced materials were ablated, and few materials were redeposited on the microchannel bed, as can be seen by comparing Figure 14b,c. When the GNPs increased to 2.5 wt.%, the ablation threshold energy was reduced, which led to melting and more material redeposition on the machined surface. This was because there was a significant amount of thick graphene surrounding

the  $\text{Al}_2\text{O}_3$  particles (see Figure 14d,e) which efficiently transferred the heat away from the melting zone, causing redeposited materials on the beds and the sidewalls of the channels. Hence, these redeposited materials slightly increased the channel depth.

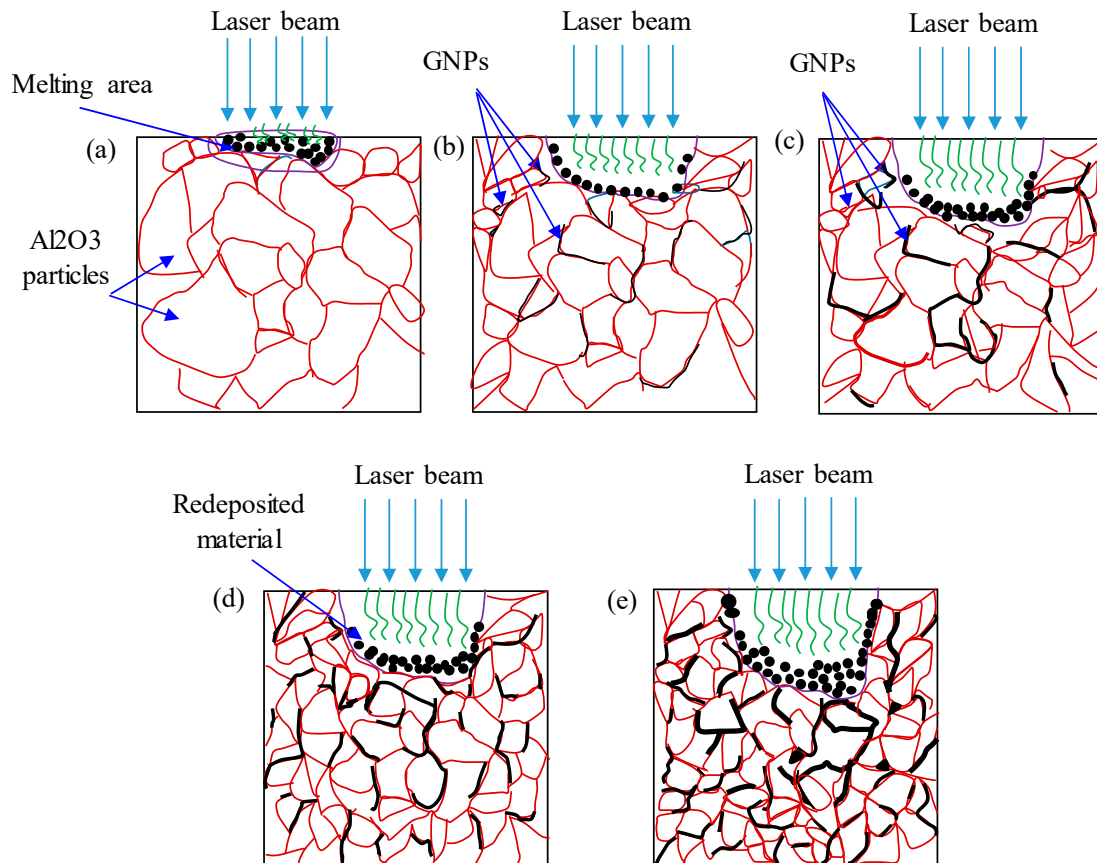


**Figure 14.** Schematic diagram of laser beam machining, (a) base  $\text{Al}_2\text{O}_3$ ; (b) 0.5 GNP/ $\text{Al}_2\text{O}_3$  nanocomposites; (c) 1 wt.% GNP/ $\text{Al}_2\text{O}_3$  nanocomposites; (d) 1.5 wt.% GNP/ $\text{Al}_2\text{O}_3$ ; (e) 2.5 wt.% GNP/ $\text{Al}_2\text{O}_3$  nanocomposites.

Figure 13b shows the impact of the graphene content with different scanning speeds on the microchannel widths of all fabricated samples. It can be seen that the results of the channel widths of the GNP/ $\text{Al}_2\text{O}_3$  nanocomposites are similar in most of the machining conditions. However, some points could be noted. In the cases of the 1.5 wt.% and 2.5 wt.% GNP specimens, the width increased as the GNP content increased from 1 wt.% to 2.5 wt.% at a scanning speed of 400 mm/s. These results can be explained as follows. The absorption of the laser energy in the GNP nanocomposites increased with the increasing graphene content, which affected the melting process and the vaporization [38]. Therefore, at low scanning speeds of 200 mm/s and 300 mm/s, there was more interaction time between the laser and materials, leading to more molten material and rapid evaporation, which resulted in increased depths and stabilization of the widths, without any changes in any of the GNP/ $\text{Al}_2\text{O}_3$  nanocomposites [49]. In the case of the high scanning speeds of 400 mm/s and 500 mm/s, it was expected that the nanocomposites with 1.5 wt.% and 2.5 wt.% GNPs would have a high absorption of energy compared to those with 0.5 wt.% and 1 wt.% GNPs, which resulted in more molten and evaporated materials from the walls and bottoms of the channels, leading to an increased width (see Figure 11a–j). However, in the case of the 2.5 wt.% GNP specimens, the width decreased at a scanning speed of 500 mm/s. This was because there was a significant amount of thick graphene surrounding the  $\text{Al}_2\text{O}_3$  particles (see Figure 14e), which efficiently transferred the heat away from the melting zone, causing redeposited materials on the sidewalls of the channels. Hence, these redeposited materials

reduced the channel width (as can clearly be seen in Figure 12e. In the case of the pure  $\text{Al}_2\text{O}_3$ , the width decreased as the scanning speed decreased. This happened because of the decrease in the absorption of energy, which led to a reduction in the melting and evaporation, resulting in a decreased width (see Figure 9a–i).

Figure 15 shows the trends of the impact of graphene contents on the microchannel depth and width at different levels of frequency. Regarding the effect of the GNPs, it can be concluded from Figure 15a that the nanocomposites reinforced with different graphene contents showed improvement in the channel depth compared to the base  $\text{Al}_2\text{O}_3$ . This trend was nearly the same as in the case of Figure 13. That is, the channel depth increased with increasing graphene contents from 0.5 wt.% to 2.5 wt.%. This is attributed to the optical absorbance and ablation threshold of the GNP/ $\text{Al}_2\text{O}_3$  nanocomposites, which can be explained as follows. The pulse energy and pulse power identify the energy density and power density of the laser beam–material interaction mode and, therefore, the amount of machined volume. Leone et al. [41] found that the energy density was reduced with an increasing pulse frequency. The differences in the channel depth for the 20 kHz results in comparison to the higher frequencies can be seen as an indication of these changes. The presence of graphene among the alumina particles led to enhanced thermal conductivity and optical absorbance of the nanocomposites. However, these nanocomposites required a lower ablation threshold pulse energy for melting the materials compared to the base alumina. With an increasing frequency from 30 to 40 kHz, less material was molten during the ablation of the  $\text{Al}_2\text{O}_3$  because the increasing frequency generated less energy. These results are in line with a reported study on the laser machining of  $\text{Al}_2\text{O}_3$  [41]. However, in the cases of the 0.5 wt.%, 1 wt.%, 1.5 wt.%, and 2.5 wt.% GNP specimens, the graphene enhanced the effects of the increasing frequency on generating a lower energy density. Therefore, more material was ablated and removed from the bottom of the channel compared to the base  $\text{Al}_2\text{O}_3$ . However, an increased channel depth was obtained by the nanocomposites with 2.5 wt.% GNP contents. Kim et al. [46] reported that  $\text{Al}_2\text{O}_3$  nanocomposites with higher CNT contents exhibited a higher ablation rate compared to those with low CNT contents due to lower light transmittance, higher thermal conductivity, and a smaller grain size. In the case of the 2.5 wt.% GNP specimens, the depth and width decreased at a frequency of 40 kHz due to the thick graphene, which conducted the heat away from the melting zone, leading to redeposited material on the wall and bottom (see Figure 14e).

Regarding the effect of graphene content on the width, as shown in Figure 15b, the results are similar, and no obvious differences were observed in the width among the 0.5 wt.%, 1 wt.%, 1.5 wt.%, 2.5 wt.% GNP specimens. In the case of the base  $\text{Al}_2\text{O}_3$ , the width sharply decreased with increasing frequency due to less energy absorbance, as explained earlier.

To show the benefits of the GNP content on the laser machining of  $\text{Al}_2\text{O}_3$ , Figure 16 is provided, which shows the improvement in the ablation depth of the GNP/ $\text{Al}_2\text{O}_3$  nanocomposites compared to the base  $\text{Al}_2\text{O}_3$ . It can be observed that the addition of GNPs enhanced the laser micromachining by increasing the ablation depth at lower and higher scanning speeds. For instance, at higher scanning speeds, the ablation depth was increased by 982%, 1004%, 1094%, and 1467% for the 0.5 wt.%, 1 wt.%, 1.5 wt.%, and 2.5 wt.% GNP/ $\text{Al}_2\text{O}_3$  nanocomposites as compared to the base  $\text{Al}_2\text{O}_3$  (see Figure 14). The results of the 2.5 wt.% GNP reinforcement exhibited the highest ablation depth during the laser beam micromachining.

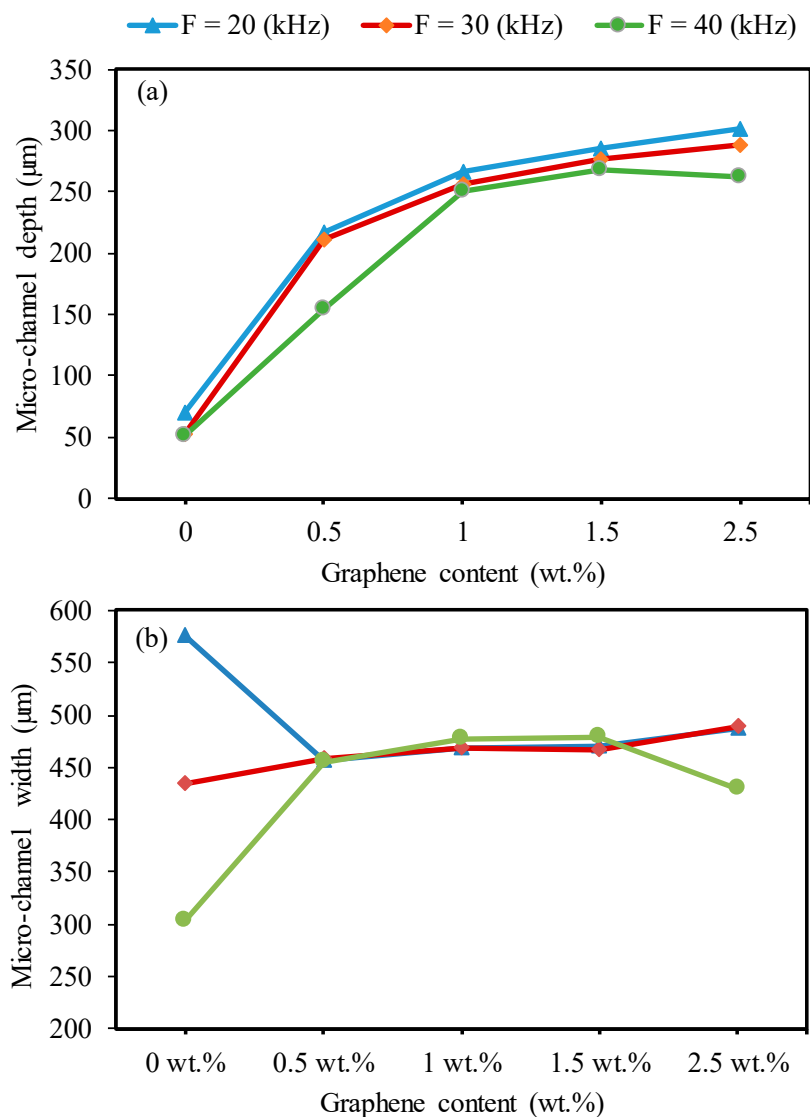


**Figure 15.** Effects of the graphene reinforcements and frequency on the microchannel depth for machining base  $\text{Al}_2\text{O}_3$  and GNP/ $\text{Al}_2\text{O}_3$  nanocomposites (SS = 300 mm/s). (a) Microchannel depth, (b) Microchannel width.

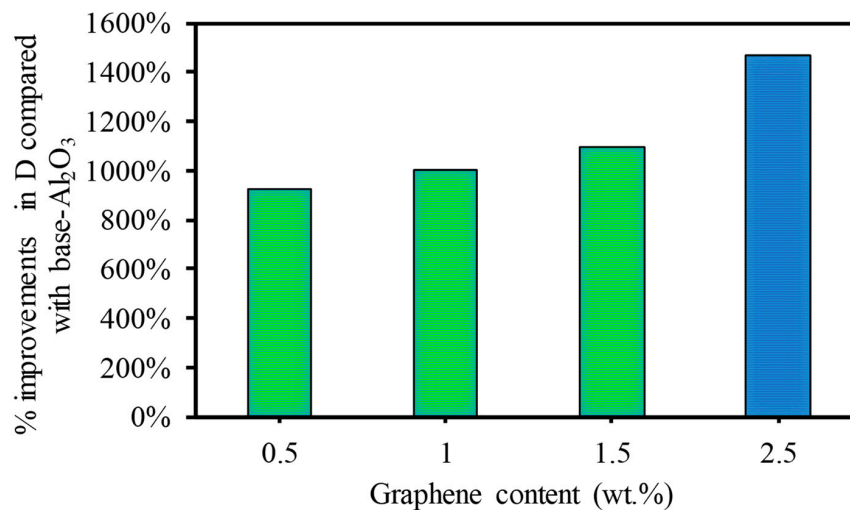


**Figure 16.** Percentage of improvement in ablation depth at a higher scanning speed of 500 mm/s.

### 3.2.3. Surface Roughness

Figure 17 illustrates the trend of the effect of graphene contents at different scanning speeds on the surface roughness of the fabricated microchannels. Regarding the impact of the graphene, it can be seen that the specimens with 0.3 wt.% and 1 wt.% GNPs had the tendency to generate the lowest surface roughness. This trend was the same as that shown in Figure 14. That is, the surface roughness increased with the increasing channel depth for the nanocomposites with 0.5 wt.%, 1 wt.%, 1.5 wt.%, and 2.5 wt.% GNPs. This is because the increase in the surface roughness with the increase in the depth occurred partly due to more molten materials, and evaporation caused the redeposited material, which affected the generated finished surface [44]. Perrie et al. [50] found that the surface roughness of the ablated microchannel increases with the machined depth due to the material redeposition. In some cases, the surface roughness tended to decrease slightly with the GNPs increasing from 1 wt.% to 1.5 wt.%. It should be noted that the formation of the laser-machined surface was mainly governed by the molten and evaporated material and was negatively affected by the redeposition of the molten material on the ablated area. The base  $\text{Al}_2\text{O}_3$  exhibited the worst surface roughness compared to all other samples. The molten material and plume of the  $\text{Al}_2\text{O}_3$  rapidly moved forward and backward inside the channel, so the propagating laser beam was absorbed and blocked by them [51]. Hence, the surface roughness was increased due to increased redeposition of molten and evaporating material.

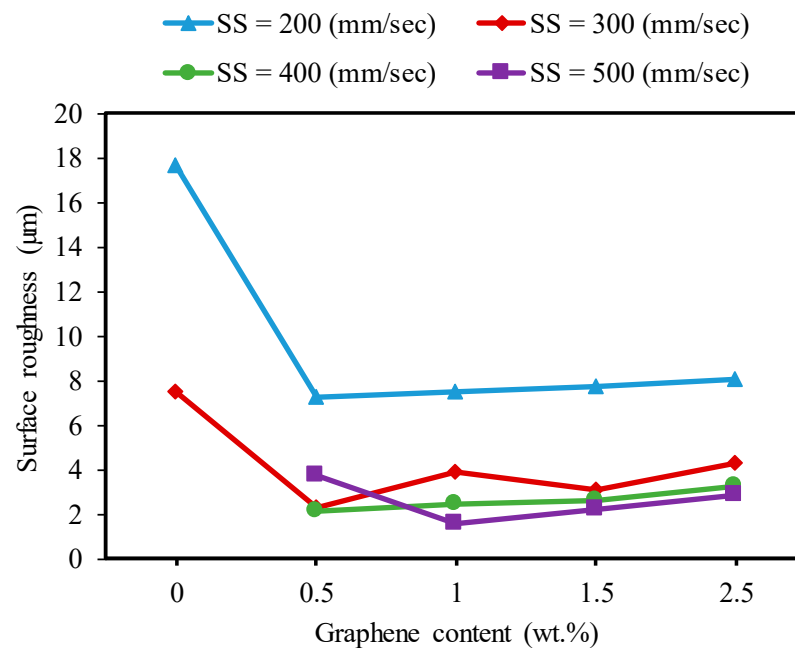


**Figure 17.** Effects of the graphene reinforcements and laser speed on the surface roughness during the micro-milling of the base  $\text{Al}_2\text{O}_3$ , and GNP/ $\text{Al}_2\text{O}_3$  nanocomposites ( $F = 30$  kHz).

Regarding the effect of the scanning speed, Figure 17 shows that surface roughness significantly decreased with the scanning speed increasing from 100 mm/s to 500 mm/s for all samples in most of the machining conditions. This is because the laser energy per unit area decreased due to the reduced interaction time between the laser beam and material with an increase in the scanning speed. This resulted in fewer molten materials being deposited on the bottom surface [44].

It can be observed that the addition of GNPs enhanced the micromachining of alumina ceramic using a fiber laser with a minimum power of 20 watts. This was achieved by improving the surface quality at lower and higher scanning speeds. For example, at a lower scanning speed of 200 mm/s, the surface roughness levels decreased by 74%, 27%, 54%, and 31% for the 0.5 wt.%, 1 wt.%, 1.5 wt.%, and 2.5 wt.% GNP/ $\text{Al}_2\text{O}_3$  nanocomposites, respectively, compared to the base  $\text{Al}_2\text{O}_3$ , as shown in Figure 18. At a higher scanning

speed of 500 mm/s, higher-quality microchannels were fabricated on all GNP/ $\text{Al}_2\text{O}_3$  nanocomposites. On the contrary, no ablated channels were fabricated on the base  $\text{Al}_2\text{O}_3$  at the higher scanning speed of 500 mm/s.

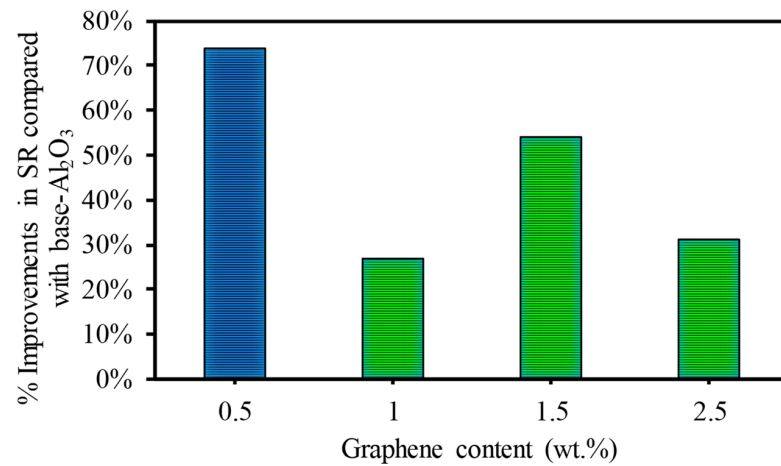


**Figure 18.** Percentage of improvement in surface roughness at a lower scanning speed of 200 mm/s.

Regarding the effects of the frequency, Figure 19 presents the effects of the GNP contents with varying frequencies on the surface roughness of the microchannels. It can be observed in Figure 19 that the surface roughness increased with increases in the GNP contents from 0.5 wt.% to 1 wt.% and then decreased when the GNP contents increased to 1.5 wt.%. After that, the surface roughness increased with increasing GNPs to 2.5 wt.%. This trend was almost the same as in the case of the channel depth shown in Figure 13a. This is attributed to differences in the material properties of the developed nanocomposites. The nanocomposites with 0.5 wt.% GNPs had the lowest surface roughness compared to the base  $\text{Al}_2\text{O}_3$  and the 1 wt.%, 1.5 wt.%, and 2.5% GNP/ $\text{Al}_2\text{O}_3$  by approximately 287%, 132%, 28%, and 165%, respectively, at a lower frequency of 20 kHz. The 2.5 wt.% GNP nanocomposite exhibited higher surface roughness than all the other specimens. This happened because of the lower ablation threshold and optical absorption in the case of the 2.5 wt.% GNP specimens, which led to a higher ablation depth with an increase in the surface roughness due to redeposited material on the bottom surface of the channel.

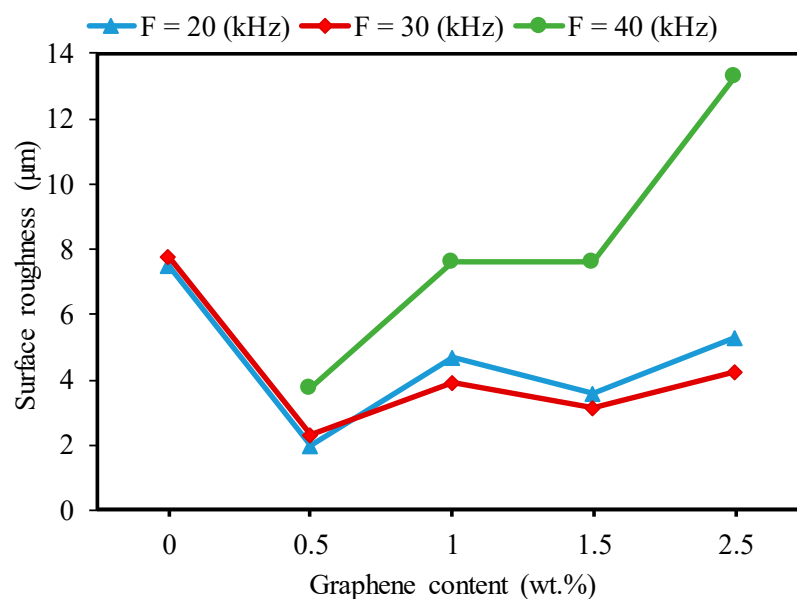


**Figure 19.** Effects of the graphene reinforcements and frequency on surface roughness during the micro-milling of the base  $\text{Al}_2\text{O}_3$  and GNP/ $\text{Al}_2\text{O}_3$  nanocomposites (SS = 300 mm/s).

In general, it can be seen in Figure 19 that the surface roughness trend increased as the frequency increased from 20 kHz to 40 kHz for the 0.5 wt.% GNP/Al<sub>2</sub>O<sub>3</sub>. The low laser energy caused more unmolten materials to be deposited at the bottom of the fabricated microchannels, which affected the roughness of the ablated surface [40,49]. In addition, Figure 20 shows that the roughness decreased by increasing the frequency to 30 kHz from 20 kHz in the case of the 1 wt.%, 1.5 wt.%, and 2.5 wt.% GNP/Al<sub>2</sub>O<sub>3</sub>. This was expected due to their higher thermal resistance, smaller grain size, and lower light transmittance compared to the 0.5 wt.% GNP/Al<sub>2</sub>O<sub>3</sub>. At the frequency of 20 kHz, excessive energy was generated, and more materials were molten and evaporated, which led to a redeposit of molten material on the surface [49].

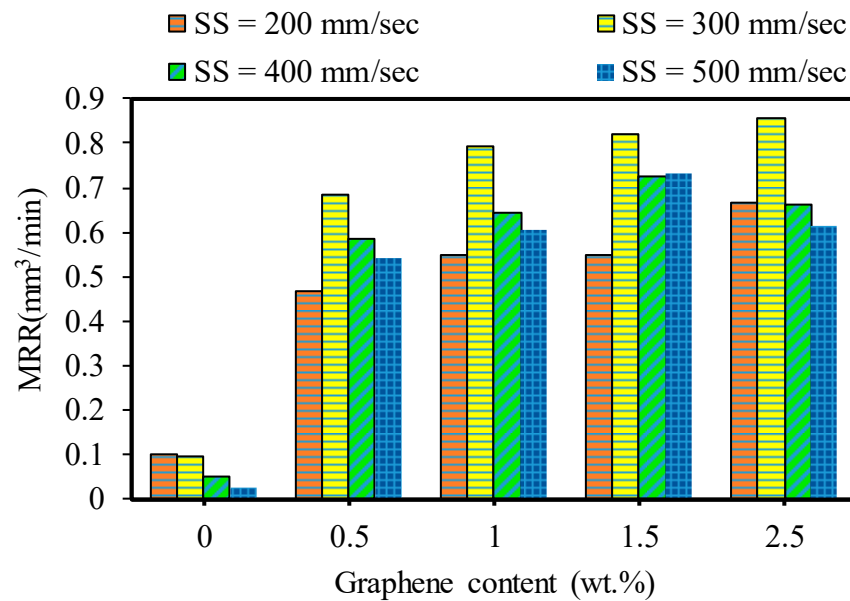


**Figure 20.** Effects of varying graphene contents with laser speed on MRR. At F = 30 kHz.

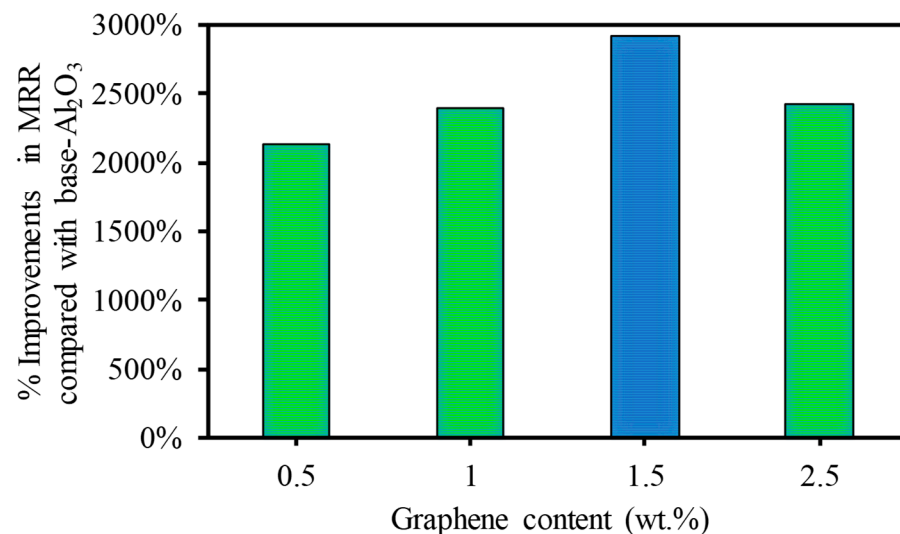
### 3.2.4. Material Removal Rate

Figure 20 shows the effects of the GNP contents and laser scanning speed on the material removal rates of the base Al<sub>2</sub>O<sub>3</sub> and GNP/Al<sub>2</sub>O<sub>3</sub> nanocomposites. From the experimental findings, it was noted that the MRR was affected by the graphene contents. The MRR results are remarkably improved in the laser micromachining of all GNP/Al<sub>2</sub>O<sub>3</sub> nanocomposites compared to the base Al<sub>2</sub>O<sub>3</sub> ceramics. It can be observed in Figure 20 that the MRR values increased with increasing GNP contents from 0.5 wt.% to 1.5 wt.% in the micro-milling of the GNP/Al<sub>2</sub>O<sub>3</sub> nanocomposites in most of the machining conditions. This is because the increase in the GNP content corresponded to lower light transmittance, higher thermal conductivity of the nanocomposite, and consequently, a higher ablation rate. In addition, this trend was almost the same as in the case of the microchannel depth. However, in the case of the 2.5 wt.% GNPs, the MRR decreased when the scanning speed increased to 500 mm/s from 300 mm/s compared to the 1.5 wt.% GNP specimens. This occurred because more material melted and was then deposited along the bottom and microchannel edges, which led to a change in the size of the machined channel (see Figures 9 and 11).

In general, it can be seen in Figure 20 that the MRR tended to decrease as the scanning speed increased from 300 mm/s to 500 mm/min for all fabricated samples. This is attributed to the fact that increasing the scanning speed led to reducing the interaction time between the laser and materials. Thus, the ablated materials decreased, resulting in a lower MRR, as discussed by [40,45]. In addition, it can be seen that the MRR increased when the scanning speed increased from 200 mm/s to 300 mm/s for all of the GNP/Al<sub>2</sub>O<sub>3</sub> samples. Although the triangular microchannels were shaped at a lower scanning speed (200 mm/s), when the scanning speed was raised to 300 mm/s and higher, the shape of the microchannels

changed from triangular to trapezoidal, with a large bottom width and less depth (see Figures 9 and 11), which indicates a higher ablation rate compared to the lower scanning speed. These results are consistent with a previous study by [45].

To show the effects of adding GNP contents on the laser micromachining of  $\text{Al}_2\text{O}_3$ , Figure 21 is presented, which shows the improvement in the MRR of the GNP/ $\text{Al}_2\text{O}_3$  nanocomposites compared to the base  $\text{Al}_2\text{O}_3$ . For example, at a lower scanning speed of 200 mm/s, the MRRs increased by 375.40%, 459.18%, 459.26%, and 581.788% for the 0.5 wt.%, 1 wt.%, 1.5 wt.%, and 2.5 wt.% GNP/ $\text{Al}_2\text{O}_3$  nanocomposites, respectively, compared to the base  $\text{Al}_2\text{O}_3$ . At a higher scanning speed of 500 mm/s, the MRRs increased by 2134%, 2391%, 2915%, and 2427% for the 0.5 wt.%, 1 wt.%, 1.5 wt.%, and 2.5 wt.% GNP/ $\text{Al}_2\text{O}_3$  nanocomposites, respectively, compared to the base  $\text{Al}_2\text{O}_3$ , as shown in Figure 21.



**Figure 21.** Percentages of improvement in MRR at a higher scanning speed of 500 mm/s.

#### 4. Conclusions

In this study, GNP/ $\text{Al}_2\text{O}_3$  matrix nanocomposites consisting of 0 wt.%, 0.5 wt.%, 1 wt.%, 1.5 wt.%, and 2.5 wt.% GNPs were successfully fabricated using powder metallurgy and the HFIHS technique. The influence of the GNP contents on the micromachining performance of the fabricated nanocomposites was investigated. Based on the experimental findings, the following conclusions are drawn:

- All of the produced GNP-based  $\text{Al}_2\text{O}_3$  nanocomposite samples exhibited high relative densities between 97.17% and 99.79%, which indicates good bonding between the GNPs and the  $\text{Al}_2\text{O}_3$  matrix without porosity or cavities.
- The hardness was moderately affected by the GNP reinforcement in the  $\text{Al}_2\text{O}_3$  matrix. Nanocomposites with 0.5 wt.% GNPs demonstrated a slight improvement in hardness by approximately 6.3% compared to the base  $\text{Al}_2\text{O}_3$ . In comparison, other nanocomposites exhibited a slight decrease in hardness.
- The SEM examination revealed that the inclusion of graphene contents had a profound influence on the surface morphology of the machined microchannels. The base  $\text{Al}_2\text{O}_3$  samples showed inferior surface quality, with pores, more redeposited materials, and microcracks. All of the GNP/ $\text{Al}_2\text{O}_3$  nanocomposites showed improvement in morphology compared to the base  $\text{Al}_2\text{O}_3$  samples. This was due to the lower ablation threshold energy of the graphene based-nanocomposites.
- The ablation depth was significantly affected by the GNP reinforcement. The GNP/ $\text{Al}_2\text{O}_3$  nanocomposites exhibited improvement in the ablation depth compared to the base  $\text{Al}_2\text{O}_3$  in all machining conditions. For example, at a scanning speed of 500 mm/s, the ablation depths increased by 9.8, 10.04, 10.9, and 14.6 times, respectively, compared to the base  $\text{Al}_2\text{O}_3$ . This was because the graphene reinforcements reduced the ablation threshold

energy required to induce the materials and increased the material removal efficiency due to higher optical absorbance, thermal conductivity, and a smaller grain size.

- The MRRs during the laser micromachining were significantly affected by the GNP reinforcement in the Al<sub>2</sub>O<sub>3</sub> matrix. For example, at a higher scanning speed, the MRRs were increased by 2134%, 2391%, 2915%, and 2427% for the 0.5 wt.%, 1 wt.%, 1.5 wt.%, and 2.5 wt.% GNP/Al<sub>2</sub>O<sub>3</sub> nanocomposites, respectively, compared to the base Al<sub>2</sub>O<sub>3</sub> ceramic.
- The roughness of the machined microchannels was affected by the GNP reinforcement. The nanocomposites with lower GNP contents exhibited the lowest surface roughness compared to the other samples. Among the machined nanocomposites, the 0.5 wt.% GNP samples showed the lowest surface roughness.
- Overall, the microchannel accuracy, surface quality, and material removal rate were significantly affected by the GNP reinforcement in the alumina matrix nanocomposites during the laser micromachining. It is worth stating again that all of the GNP-reinforced alumina matrix nanocomposites showed improved micromachining performance compared to the unreinforced samples. Moreover, by comparing the influence of the GNP reinforcements on the surface roughness and surface morphology, the nanocomposites with 0.3 wt.% and 1wt.% GNPs largely showed better performance in most of the machining conditions, while the nanocomposites with 1.5 wt.% and 2.5 wt.% GNPs showed better machining performance regarding the ablation rate and material removal rate. The results show that GNP/Al<sub>2</sub>O<sub>3</sub> nanocomposites can be machined with very good quality using a very ordinary 20 W fiber laser. In contrast, pure Al<sub>2</sub>O<sub>3</sub> could not be machined using the same low-power and low-budget laser system. This helps in achieving the clean and sustainable manufacturing goals with reduced energy consumption for clean environment.

**Author Contributions:** Conceptualization, M.M.N.; methodology, M.M.N. and S.A.; software, M.M.N.; validation, M.M.N., S.A. and A.M.A.-S.; formal analysis, M.M.N., S.A. and A.M.A.-S.; investigation, M.M.N., S.A., K.N.A., A.D. and M.H.A.; resources, A.M.A.-S.; data curation, M.M.N. and S.A.; writing—original draft preparation, M.M.N.; writing—review and editing, M.M.N., S.A. and K.N.A.; visualization, M.M.N.; supervision, S.A., A.M.A.-S. and K.N.A. All authors have read and agreed to the published version of the manuscript.

**Funding:** Deputyship for Research & Innovation, Ministry of Education in Saudi Arabia project no. (IFKSURG-2-804).

**Data Availability Statement:** The data are available on request from corresponding author.

**Acknowledgments:** The authors extend their appreciation to the Deputyship for Research & Innovation, Ministry of Education in Saudi Arabia for funding this research work through the project no. (IFKSURG-2-804).

**Conflicts of Interest:** The authors declare no conflict of interest.

## References

1. Ahmad, I.; Anwar, S.; Xu, F.; Zhu, Y. Tribological Investigation of Multilayer Graphene Reinforced Alumina Ceramic Nanocomposites. *J. Tribol.* **2019**, *141*, 022002. [[CrossRef](#)]
2. Brandner, J.J. Fabrication of Microreactors Made from Metals and Ceramics. In *Microreactors in Organic Synthesis and Catalysis*; Wiley-VCH Verlag GmbH & Co. KGaA: Weinheim, Germany, 2008; pp. 1–17.
3. Abdo, B.M.A.; Anwar, S.; El-Tamimi, A.M.; Nasr, E.A. Experimental Analysis on the Influence and Optimization of  $\mu$ -RUM Parameters in Machining Alumina Bioceramic. *Materials* **2019**, *12*, 616. [[CrossRef](#)] [[PubMed](#)]
4. Sommers, A.; Wang, Q.; Han, X.; T'Joel, C.; Park, Y.; Jacobi, A. Ceramics and Ceramic Matrix Composites for Heat Exchangers in Advanced Thermal Systems—A Review. *Appl. Therm. Eng.* **2010**, *30*, 1277–1291. [[CrossRef](#)]
5. Sternitzke, M.; Derby, B.; Brook, R.J. Alumina/Silicon Carbide Nanocomposites by Hybrid Polymer/Powder Processing: Microstructures and Mechanical Properties. *J. Am. Ceram. Soc.* **1998**, *81*, 41–48. [[CrossRef](#)]
6. Morisada, Y.; Miyamoto, Y.; Takaura, Y.; Hirota, K.; Tamari, N. Mechanical Properties of SiC Composites Incorporating SiC-Coated Multi-Walled Carbon Nanotubes. *Int. J. Refract. Met. Hard Mater.* **2007**, *25*, 322–327. [[CrossRef](#)]

7. Grigoriev, S.; Peretyagin, P.; Smirnov, A.; Solís, W.; Díaz, L.A.; Fernández, A.; Torrecillas, R. Journal of the European Ceramic Society Effect of Graphene Addition on the Mechanical and Electrical Properties of Al<sub>2</sub>O<sub>3</sub>-SiCw Ceramics. *J. Eur. Ceram. Soc.* **2017**, *37*, 2473–2479. [[CrossRef](#)]
8. Llorca, J.; Elices, M.; Celemin, J.A. Toughness and Microstructural Degradation at High Temperature in SiC Fiber-Reinforced Ceramics. *Acta Mater.* **1998**, *46*, 2441–2453. [[CrossRef](#)]
9. Fu, Y.; Gu, Y.W.; Du, H. SiC Whisker Toughened Al<sub>2</sub>O<sub>3</sub>-(Ti,W)C Ceramic Matrix Composites. *Scr. Mater.* **2001**, *44*, 111–116. [[CrossRef](#)]
10. Ahmad, I.; Islam, M.; Sayed, H.; Subhani, T.; Abdelrazek, K.; Almajid, A.A.; Yazdani, B.; Zhu, Y. Toughening Mechanisms and Mechanical Properties of Graphene Nanosheet-Reinforced Alumina. *Mater. Des.* **2015**, *88*, 1234–1243. [[CrossRef](#)]
11. Shah, W.A.; Luo, X.; Guo, C.; Rabiou, B.I.; Huang, B.; Yang, Y.Q. Preparation and Mechanical Properties of Graphene-Reinforced Alumina-Matrix Composites. *Chem. Phys. Lett.* **2020**, *754*, 137765. [[CrossRef](#)]
12. Nasr, M.M.; Anwar, S.; Al-Samhan, A.M.; Abdo, H.S.; Dabwan, A. On the Machining Analysis of Graphene Nanoplatelets Reinforced Ti6Al4V Matrix Nanocomposites. *J. Manuf. Process.* **2021**, *61*, 574–589. [[CrossRef](#)]
13. Cygan, T.; Petrus, M.; Wozniak, J.; Cygan, S.; Teklińska, D.; Kostecki, M.; Jaworska, L.; Olszyna, A. Mechanical Properties and Tribological Performance of Alumina Matrix Composites Reinforced with Graphene-Family Materials. *Ceram. Int.* **2020**, *46*, 7170–7177. [[CrossRef](#)]
14. Rivero-Antúnez, P.; Zamora-Ledezma, C.; Sánchez-Bajo, F.; Moreno-López, J.C.; Anglaret, E.; Morales-Flórez, V. Sol-Gel Method and Reactive SPS for Novel Alumina-Graphene Ceramic Composites. *J. Eur. Ceram. Soc.* **2023**, *43*, 1064–1077. [[CrossRef](#)]
15. Shah, W.A.; Luo, X.; Yang, Y.Q. Mechanical and Thermal Properties of Spark Plasma Sintered Al<sub>2</sub>O<sub>3</sub>-Graphene-SiC Hybrid Composites. *Ceram. Int.* **2023**, *49*, 7987–7995. [[CrossRef](#)]
16. Kuşoğlu, I.M.; Çavdar, U.; Altıntaş, A. The Effects of Graphene Nanoplatelet Addition to in Situ Compacted Alumina Nanocomposites Using Ultra-High Frequency Induction Sintering System. *J. Aust. Ceram. Soc.* **2020**, *56*, 233–241. [[CrossRef](#)]
17. Nieto, A.; Bisht, A.; Lahiri, D.; Zhang, C.; Agarwal, A. Graphene Reinforced Metal and Ceramic Matrix Composites: A Review. *Int. Mater. Rev.* **2017**, *62*, 241–302. [[CrossRef](#)]
18. Mudra, E.; Shepa, I.; Hrubovcakova, M.; Koribanich, I.; Medved, D.; Kovalcikova, A.; Vojtko, M.; Dusza, J. Highly Wear-Resistant Alumina/Graphene Layered and Fiber-Reinforced Composites. *Wear* **2021**, *484–485*, 204026. [[CrossRef](#)]
19. Shah, W.A.; Luo, X.; Rabiou, B.I.; Huang, B.; Yang, Y.Q. Toughness Enhancement and Thermal Properties of Graphene-CNTs Reinforced Al<sub>2</sub>O<sub>3</sub> Ceramic Hybrid Nanocomposites. *Chem. Phys. Lett.* **2021**, *781*, 138978. [[CrossRef](#)]
20. Duntu, S.H.; Hukapati, K.; Ahmad, I.; Islam, M.; Boakye-Yiadom, S. Deformation and Fracture Behaviour of Alumina-Zirconia Multi-Material Nanocomposites Reinforced with Graphene and Carbon Nanotubes. *Mater. Sci. Eng. A* **2022**, *835*, 142655. [[CrossRef](#)]
21. Wang, X.; Zhao, J.; Cui, E.; Tian, X.; Sun, Z. Effect of Interfacial Structure on Mechanical Properties of Graphene Reinforced Al<sub>2</sub>O<sub>3</sub>-WC Matrix Ceramic Composite. *Nanomaterials* **2021**, *11*, 1374. [[CrossRef](#)]
22. Liang, L.; Huang, C.; Wang, C.; Sun, X.; Yang, M.; Wang, S.; Cheng, Y.; Ning, Y.; Li, J.; Yin, W.; et al. Ultratough Conductive Graphene/Alumina Nanocomposites. *Compos. Part A Appl. Sci. Manuf.* **2022**, *156*, 106871. [[CrossRef](#)]
23. He, T.; Li, J.; Wang, L.; Zhu, J.; Jiang, W. Preparation and Consolidation of Alumina/Graphene Composite Powders. *Mater. Trans.* **2009**, *50*, 749–751. [[CrossRef](#)]
24. Wang, K.; Wang, Y.; Fan, Z.; Yan, J.; Wei, T. Preparation of Graphene Nanosheet/Alumina Composites by Spark Plasma Sintering. *Mater. Res. Bull.* **2011**, *46*, 315–318. [[CrossRef](#)]
25. Porwal, H.; Tatarko, P.; Grasso, S.; Khaliq, J.; Dlouhý, I.; Reece, M.J. Graphene Reinforced Alumina Nano-Composites. *Carbon* **2013**, *64*, 359–369. [[CrossRef](#)]
26. Chen, Y.F.; Bi, J.Q.; Yin, C.L.; You, G.L. Microstructure and Fracture Toughness of Graphene Nanosheets/Alumina Composites. *Ceram. Int.* **2014**, *40*, 13883–13889. [[CrossRef](#)]
27. Liu, X.; Fan, Y.-C.; Li, J.-L.; Wang, L.-J.; Jiang, W. Preparation and Mechanical Properties of Graphene Nanosheet Reinforced Alumina Composites. *Adv. Eng. Mater.* **2015**, *17*, 28–35. [[CrossRef](#)]
28. Kim, W.; Oh, H.S.; Shon, I.J. The Effect of Graphene Reinforcement on the Mechanical Properties of Al<sub>2</sub>O<sub>3</sub>ceramics Rapidly Sintered by High-Frequency Induction Heating. *Int. J. Refract. Met. Hard Mater.* **2015**, *48*, 376–381. [[CrossRef](#)]
29. Liu, J.; Yang, Y.; Hassanin, H.; Jumbu, N.; Deng, S.; Zuo, Q.; Jiang, K. Graphene-Alumina Nanocomposites with Improved Mechanical Properties for Biomedical Applications. *ACS Appl. Mater. Interfaces* **2016**, *8*, 2607–2616. [[CrossRef](#)]
30. Ahmad, I.; Subhani, T.; Wang, N.; Zhu, Y. Thermophysical Properties of High-Frequency Induction Heat Sintered Graphene Nanoplatelets/Alumina Ceramic Functional Nanocomposites. *J. Mater. Eng. Perform.* **2018**, *27*, 2949–2959. [[CrossRef](#)]
31. Fan, Y.; Wang, L.; Li, J.; Li, J.; Sun, S.; Chen, F.; Chen, L.; Jiang, W. Preparation and Electrical Properties of Graphene Nanosheet/Al<sub>2</sub>O<sub>3</sub> Composites. *Carbon* **2010**, *48*, 1743–1749. [[CrossRef](#)]
32. Porwal, H.; Kasiarova, M.; Tatarko, P.; Grasso, S.; Dusza, J.; Reece, M.J. Scratch Behaviour of Graphene Alumina Nanocomposites. *Adv. Appl. Ceram.* **2015**, *114*, S34–S41. [[CrossRef](#)]
33. Yazdani, B.; Porwal, H.; Xia, Y.; Yan, H.; Reece, M.J.; Zhu, Y. Role of Synthesis Method on Microstructure and Mechanical Properties of Graphene/Carbon Nanotube Toughened Al<sub>2</sub>O<sub>3</sub> Nanocomposites. *Ceram. Int.* **2015**, *41*, 9813–9822. [[CrossRef](#)]

34. Sung, J.W.; Kim, K.H.; Kang, M.C. Effects of Graphene Nanoplatelet Contents on Material and Machining Properties of GNP-Dispersed Al<sub>2</sub>O<sub>3</sub> Ceramics for Micro-Electric Discharge Machining. *Int. J. Precis. Eng. Manuf.-Green Technol.* **2016**, *3*, 247–252. [[CrossRef](#)]
35. Nieto, A.; Zhao, J.M.; Han, Y.H.; Hwang, K.H.; Schoenung, J.M. Microscale tribological behavior and in vitro biocompatibility of graphene nanoplatelet reinforced alumina. *J. Mech. Behav. Biomed. Mater.* **2016**, *61*, 122–134. [[CrossRef](#)] [[PubMed](#)]
36. Liu, J.; Camfield, R. Machinability Experimental Study of Sintered Alumina (Al<sub>2</sub>O<sub>3</sub>) Ceramics Material by Chemical Vapor Deposition Diamond Coating Milling Tools. *Proc. Inst. Mech. Eng. Part B J. Eng. Manuf.* **2015**, *229*, 1535–1546. [[CrossRef](#)]
37. Abdo, B.M.A.; Ahmed, N.; El-Tamimi, A.M.; Anwar, S.; Alkhalefeh, H.; Nasr, E.A. Laser Beam Machining of Zirconia Ceramic: An Investigation of Micro-Machining Geometry and Surface Roughness. *J. Mech. Sci. Technol.* **2019**, *33*, 1817–1831. [[CrossRef](#)]
38. Lee, J.Y.; Kang, M.C.; Kim, K.H.; Park, W.I.; Cho, S.H. Effects of Optical Absorbance with Ablation Characteristics in Femtosecond Laser Irradiation of Carbon Reinforced Al<sub>2</sub>O<sub>3</sub> Composites. *Adv. Appl. Ceram.* **2016**, *115*, 123–128. [[CrossRef](#)]
39. López-Pernía, C.; Muñoz-Ferreiro, C.; González-Orellana, C.; Morales-Rodríguez, A.; Gallardo-López, Poyato, R. Optimizing the Homogenization Technique for Graphene Nanoplatelet/Yttria Tetragonal Zirconia Composites: Influence on the Microstructure and the Electrical Conductivity. *J. Alloys Compd.* **2018**, *767*, 994–1002. [[CrossRef](#)]
40. Abdo, B.M.A.; Anwar, S.; El-Tamimi, A.M.; Alahmari, A.M.; Abouel Nasr, E. Laser Micro-Milling of Bio-Lox Forte Ceramic: An Experimental Analysis. *Precis. Eng.* **2018**, *53*, 179–193. [[CrossRef](#)]
41. Leone, C.; Genna, S.; Tagliaferri, F.; Palumbo, B.; Dix, M. Experimental Investigation on Laser Milling of Aluminium Oxide Using a 30 W Q-Switched Yb:YAG Fiber Laser. *Opt. Laser Technol.* **2016**, *76*, 127–137. [[CrossRef](#)]
42. Zhang, X.; Ji, L.; Zhang, L.; Wang, W.; Yan, T. Polishing of Alumina Ceramic to Submicrometer Surface Roughness by Picosecond Laser. *Surf. Coat. Technol.* **2020**, *397*, 125962. [[CrossRef](#)]
43. Preusch, F.; Adelman, B.; Hellmann, R. Micromachining of AlN and Al<sub>2</sub>O<sub>3</sub> Using Fiber Laser. *Micromachines* **2014**, *5*, 1051–1060. [[CrossRef](#)]
44. Deng, D.; Xie, Y.; Chen, L.; Chen, X. Experimental Investigation on Laser Micromilling of SiC Microchannels. *Int. J. Adv. Manuf. Technol.* **2019**, *101*, 9–21. [[CrossRef](#)]
45. Agarwal, B.D.; Broutman, L.J.; Chandrashekhara, K. *Analysis and Performance of Fiber Composites*; John Wiley & Sons: Hoboken, NJ, USA, 2006.
46. Kim, K.R.; Choi, B.D.; Yi, J.S.; Cho, S.H.; Choa, Y.H.; Shin, D.S.; Bae, D.H.; Kang, M.C.; Jeong, Y.K. Laser Micromachining of CNT/Fe/Al<sub>2</sub>O<sub>3</sub> Nanocomposites. *Trans. Nonferrous Met. Soc. China* **2009**, *19*, s189–s193. [[CrossRef](#)]
47. Kumari, L.; Zhang, T.; Du, G.H.; Li, W.Z.; Wang, Q.W.; Datye, A.; Wu, K.H. Thermal Properties of CNT-Alumina Nanocomposites. *Compos. Sci. Technol.* **2008**, *68*, 2178–2183. [[CrossRef](#)]
48. Li, Q.; Zhang, Y.; Gong, H.; Sun, H.; Li, T.; Guo, X.; Ai, S. Effects of Graphene on the Thermal Conductivity of Pressureless-Sintered SiC Ceramics. *Ceram. Int.* **2015**, *41*, 13547–13552. [[CrossRef](#)]
49. Xing, Y.; Liu, L.; Wu, Z.; Wang, X.; Huang, P.; Tang, L. Fabrication and Characterization of Micro-Channels on Al<sub>2</sub>O<sub>3</sub>/TiC Ceramic Produced by Nanosecond Laser. *Ceram. Int.* **2018**, *44*, 23035–23044. [[CrossRef](#)]
50. Perrie, W.; Rushton, A.; Gill, M.; Fox, P.; O'Neill, W. Femtosecond Laser Micro-Structuring of Alumina Ceramic. *Appl. Surf. Sci.* **2005**, *248*, 213–217. [[CrossRef](#)]
51. Kim, K.R.; Kim, J.H.; Kim, K.H.; Niihara, K.; Jeong, Y.K. Laser Microfabrication of Alumina-Silicon Carbide Nanocomposites. *J. Ceram. Process. Res.* **2008**, *9*, 421–424.

**Disclaimer/Publisher's Note:** The statements, opinions and data contained in all publications are solely those of the individual author(s) and contributor(s) and not of MDPI and/or the editor(s). MDPI and/or the editor(s) disclaim responsibility for any injury to people or property resulting from any ideas, methods, instructions or products referred to in the content.